Science & Technology Facilities Council

Technical Report
RAL-TR-2017-001

SCARF Annual Report 2015-2016

D Ross

January 2017

©2017 Science and Technology Facilities Council

This work is licensed under a Creative Commons Attribution 3.0 Unported License.

Enquiries concerning this report should be addressed to:

RAL Library
STFC Rutherford Appleton Laboratory
Harwell Oxford
Didcot
OX11 0QX

Tel: +44(0)1235 445384
Fax: +44(0)1235 446403
email: libraryral@stfc.ac.uk

Science and Technology Facilities Council reports are available online at: http://epubs.stfc.ac.uk

ISSN 1358-6254

Neither the Council nor the Laboratory accept any responsibility for loss or damage arising from the use of information contained in any of their reports or in any communication about their tests or investigations.

SCARF Annual Report 2015-2016

Version: 1.0

Date: 13/02/2017

Edited by Derek Ross (derek.ross@stfc.ac.uk) 01235 445651

Content written by the respective authors

Date	Revision	Changes
13/02/17	1.0	Release version
06/02/17	0.3	Completed editing of science highlights
17/11/16	0.2	Initial import of science highlights
12/10/16	0.1	Initial document

Abstract

Annual Report on the Usage and Scientific Impact of the SCARF Service

Dissemination

This is a public document

1 SCARF SERVICE

SCARF is a High Performance Cluster for STFC staff, Facilities (ISIS, DIAMOND, CLF) and their users. The SCARF Service was started in 2004 and has been upgraded year on year and now represents a significant capital investment in High Performance Computing. Overall SCARF now has over 5400 CPU cores, 25TB memory and 160TB of disk space (Details in Appendix 1).

This report covers the year 2015-16 and outlines the research that SCARF has enabled.

1.1 SCARF Usage by Department

Each time a researcher uses the SCARF service the CPU time used is recorded. Jobs submitted to SCARF used 31.6 million CPU Hours during 2015-16.

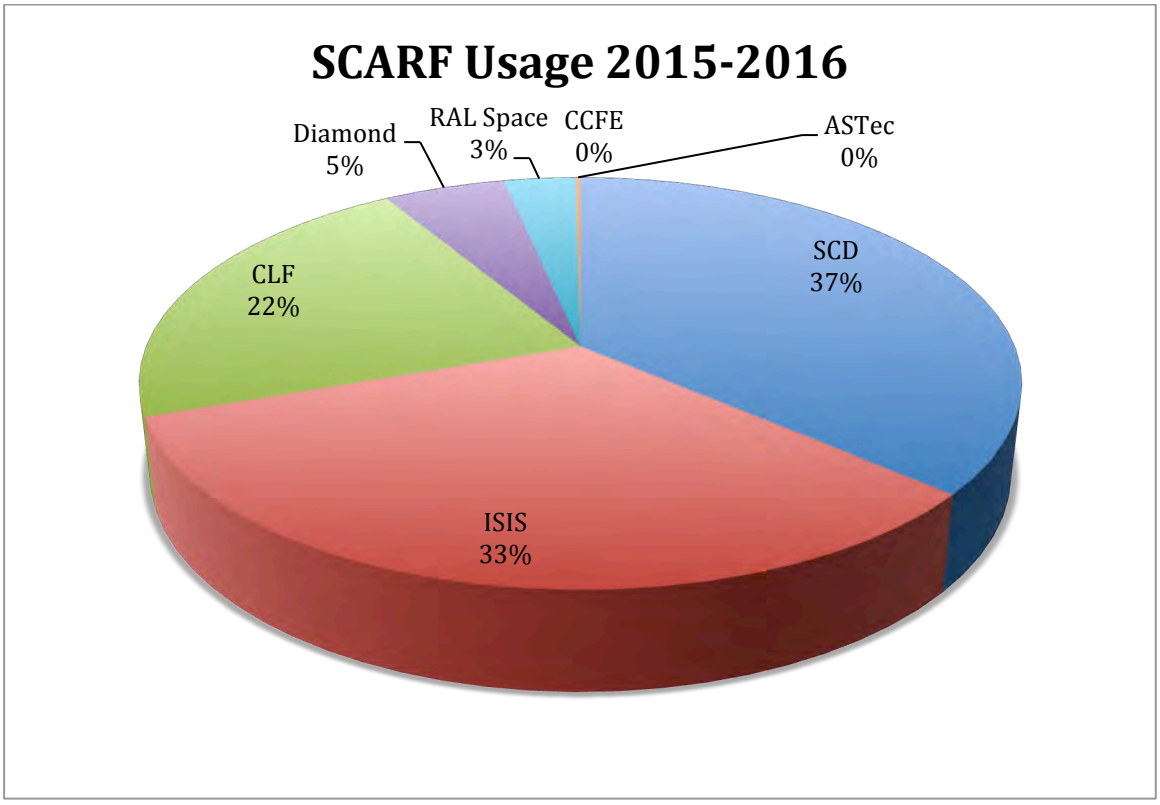

Figure 1.1.1: Pie chart showing percentage usage of the SCARF service by department

It is clear from the usage chart that ISIS, CLF and Scientific Computing are the heaviest users of SCARF. The table below shows the number of active users affiliated with e.g. Staff, collaborating with or using the facilities of various STFC departments and significant external facilities such as Diamond or CCFE. We have stopped counting External access users separately; instead they are now counted under the STFC Department they are collaborating with.

	2015-16			2014-15			2013-14		
Dept	**Active Users**	**CPU hrs**	**%**	**Active Users**	**CPU hrs**	**%**	**Active Users**	**CPU hrs**	**%**
SCD	52	11394064.3	36.2	49	8210127.49	31.4	37	8980895.60	47.1
ISIS	54	10413282.5	33.1	31	4987828.88	19.1	29	2926677.53	15.4
External	n/a	n/a	n/a	37	6716465.17	25.7	22	4748211.01	24.9
CLF	43	6829135.47	21.7	19	5298080.49	20.3	29	2010153.36	10.5
DIAMOND	3	1653629.8	5.2	6	141874.42	0.54	3	5970.4	0.0
ASTEC	2	58299.64	0.19	3	45641.77	0.17	3	112843.12	0.6
RAL Space	5	989267.1	3.1	4	718069.17	2.8	2	267668.469	1.4
CCFE	1	81.59	0	0	0	0	0	0	0
Totals	**165**	**31451022**	**100**	**149**	**26118087**	**100**	**128**	**19055284**	**100**

Figure 1.1.2: Table displaying detailed usage from 2015-16 comparing with 2014-15 and 2013-14

A significant amount of computational resource has been used on SCARF; section 3 highlights some of the scientific achievements that have been enabled.

1.2 SCARF Availability

The aim is to keep SCARF available to users as much as possible, this year we took the entire cluster down to upgrade the batch system software, as the existing software could not handle newer operating systems. There was also an issue with the air-conditioning in the machine room where SCARF is hosted, requiring the cluster to be shutdown at short notice.

1.3 SCARF Developments 2015-16

Major SCARF Developments are listed below. A more detailed list can be found in Appendix 5

- New capacity added in June 2016
  - 480 Intel E5-2650v3 CPU cores for use by CLF Plasma Physics collaborators
  - 240 Intel E5-2650v3 CPU cores for use by the IBIS collaboration
  - 400 Intel E5-2650v3 CPU cores for general use Future Developments

The hardware procurement of SCARF17 is currently in progress, it is expected to be delivered by the end of March and to enter service in mid-2017.

7 Panasas PAS-11 shelves provide SCARF's storage for home, work and scratch areas; these are now end-of-life and are scheduled to be replaced in the next financial year.

We plan to migrate SCARF to the RHEL 7 operating system in 2017, bringing updated versions of libraries and tools.

1.4 Help and Support

For any queries concerning the SCARF service please email the SCARF Helpdesk

scarf@hpc-support.rl.ac.uk

2 PUBLICATIONS AND PRESENTATIONS

2.1 Publications

A list of publications is given in Appendix 3. A way of estimating the impact that SCARF has had is to analyse the Journal Impact Factor using the Journal Citation Reports published by Thomson Reuters (2015). The average Impact Factor for Journals published as a result of using SCARF is 5.47.

2.2 Presentations

Scientists have presented their work at 10 international conferences (Appendix 3). This helps to demonstrate that the science enabled by SCARF is world class.

3 SCIENCE HIGHLIGHTS

3.1 Effect of Monoglycerides and Fatty Acids on a Ceramide Bilayer

Anna Akinshina[1], Chinmay Das[2] and Massimo G. Noro[3],
Physical Chemistry Chemical Physics, **2016**, 18, 17446 - 17460 (open access)
http://pubs.rsc.org/en/content/articlepdf/2016/cp/c6cp01238h

1. Institute of Skin Integrity and Infection Prevention, School of Human and Health
2. Sciences, University of Huddersfield, HD1 3DH, Huddersfield, UK
3. School of Mathematics, University of Leeds, Leeds, LS2 9JT, UK
4. Unilever R&D Port Sunlight, Quarry Road East, Bebington, Wirral, CH63 3JW, UK

Skin is the largest organ in our body. The major function of the skin is protection our body from the invasion of external pathogens and toxins and from internal water loss. Skin is also an important route for delivery of therapeutic agents into the body from topical applications. Delivery of drugs through the skin is a very attractive and rapidly growing approach to drug delivery because it provides convenient, effective and pain-free route of administration of therapeutic agents. The main challenge in dermal medication is penetrating the skin barrier.

Stratum Corneum (SC), the topmost layer of skin, consists of nonviable keratin-rich cells (corneocytes) embedded in rigid lipid multilayers comprised mostly of ceramides (CER), cholesterol (CHOL) and fatty acids (FA). SC lipid phase is the main barrier against passive permeation and therefore the understanding of the structure and properties of the skin lipids is of key importance.

Monoglycerides and fatty acids, naturally present in the stratum corneum, are commonly used in pharmaceutical, cosmetic and health care formulations. This research is focused on how the oil additives get incorporated into the skin lipids from topical applications and once incorporated, how they affect the properties and integrity of the lipid matrix. We have used ceramide bilayer as a model for skin lipid phase and investigated the effect of six different natural oil ingredients at multiple concentrations. The study includes the oils with the same tail length (C18) but a varying degree of saturation. The hydrogen bonding between different components, lipid tail order, lipid packing and bilayer rigidity is explored. The simulation systems consist of ~ 20,000 atomic sites each.

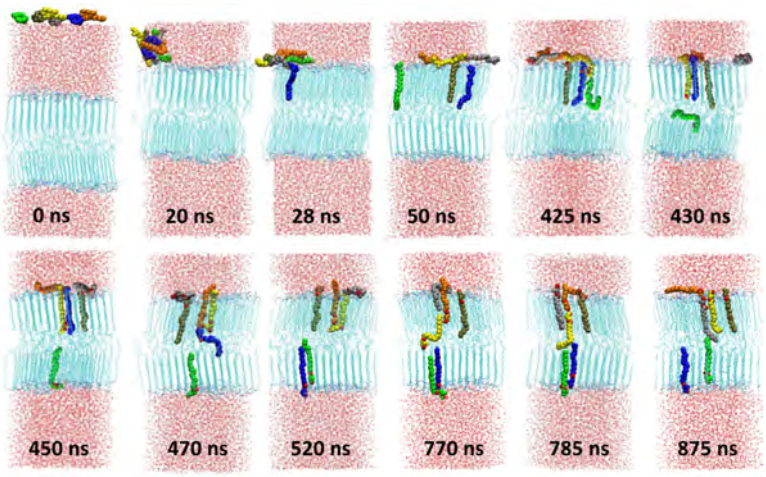

Figure 3.1.1: Spontaneous permeation of monoolein (MO) molecules. The MO molecules are coloured differently in order to visualise the dynamics and location of the individual molecules.

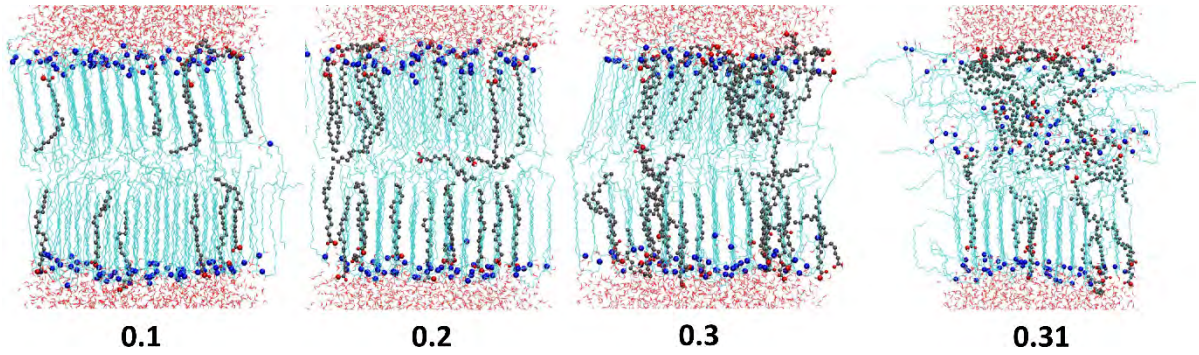

Figure 3.1.2: Snapshots of ceramide 2 (CER2) – linoleic acid (LA) bilayers at different LA mole fractions, X_{LA}, indicated on the image. Ceramide 2 tails are shown as cyan lines and LA tails as grey balls and sticks. Red balls are ester oxygen (O) atoms from LA head groups and blue balls are nitrogen (N) atoms from the CER2 head groups. Water molecules are shown as light grey and red lines, above and below the bilayers. The figure clearly illustrates the disruption of the mixed bilayer when the concentration of added linoleic acid (containing 2 cis-double bonds) exceeds 31%.

The simulations were performed with the help of STFC (SCARF) computational facilities.

3.2 Atomistic and coarse-grained study of phase behaviour of non-ionic chromonic molecules. The case of TP6EO2M.

Anna Akinshina[1], Andrey V. Brukhno[2], Andrew J. Masters[3], and Paola Carbone[3]

1. Institute of Skin Integrity & Infection Prevention, School of Human & Health Sciences, University of Huddersfield, HD1 3DH, Huddersfield, UK
2. SCD, STFC Daresbury Laboratory, Sci-Tech Daresbury, Keckwick Lane, Daresbury
3. Cheshire WA4 4AD
4. School of Chemical Engineering & Analytical Science, The University of Manchester, Oxford Road, Manchester, M13 9PL

Chromonics are attractive and interesting class of lyotropic liquid crystals with a variety of applications. Many chromonics are known as dyes (used in food, cosmetic, textile, paper industries), some of them are used as drugs and others have potential applications as media for alignment of nanorods, for thin film fabrication, and for real-time microbial sensors. Chromonic molecules are usually composed of poly-aromatic discs surrounded by solubilising groups. This characteristic molecular structure leads to aggregation in aqueous solution, most usually into molecular stacks. At higher concentrations stacks self-organise to form lyotropic mesophases. Aggregation occurs in the absence of a critical micelle concentration, and often at extremely low concentrations.

Non-ionic chromonic mesogen 2,3,6,7,10,11-hexa-(1,4,7-trioxa-octyl)-triphenylene (TP6EO2M) is a symmetrical disc-shaped molecule composed of a central poly-aromatic core (a triphenylene ring) functionalized by six hydrophilic ethyleneoxy (EO) chains. (Fig 3.2.1) These molecules aggregate face-to-face into stacks even in very dilute solution.

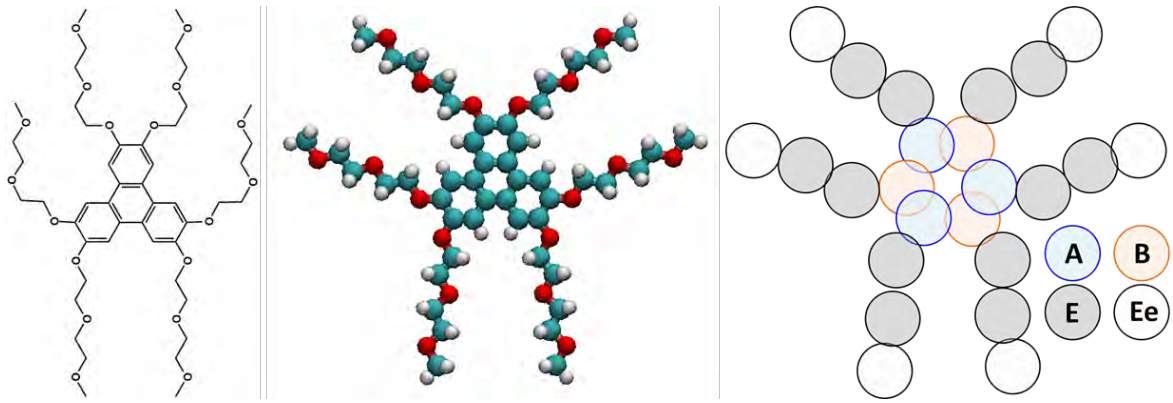

Figure 3.2.1: (A) The chemical structure, (B) atomistic model and (C) coarse-grained model of TP6EO2M used in this study. Colour code in (B): turquoise – carbons, red – oxygens, white – hydrogens.

An explicit solvent coarse-grained model for the non-ionic chromonic mesogen TP6EO2M has been developed and explored in a wide range of concentrations. The coarse-grained model of the molecule was obtained using Iterative Boltzmann Inversion method applied to a full atom system

consisting of a stack of 20 TP6EO2M molecules. The atomistic simulations were performed using OPLS-AA force field and SPC water model. The results were validated using atomistic simulations for small systems and experimental data for mesophases. Exploring the local properties of the self-assembled stacks we observe good agreement between the atomistic and CG models. The phase behaviour of mesophases is in qualitative agreement with experimental data.

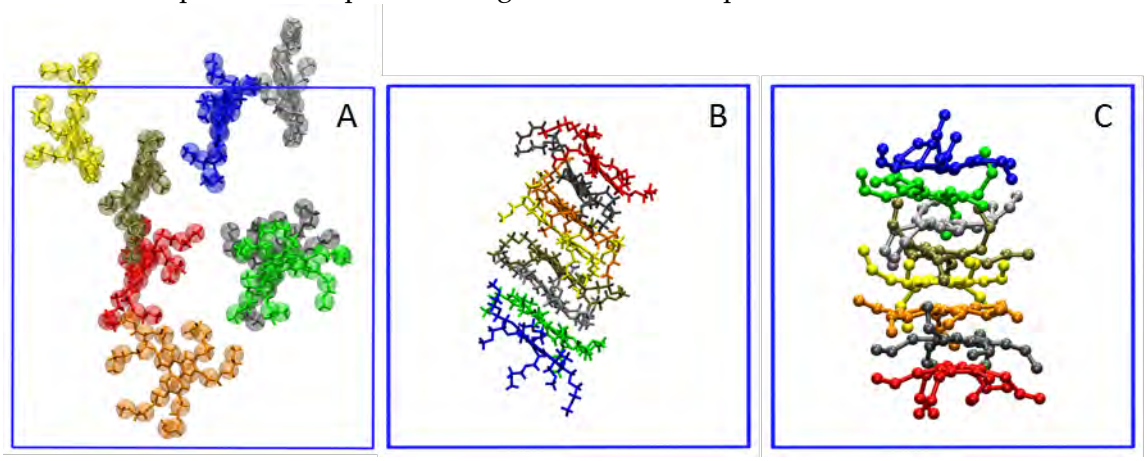

Figure 3.2.2: Snapshots from self-assembly of 8 TP6EO2M molecules into a stack. (A) Starting configuration with randomly placed molecules. (B) Atomistic simulation and (C) coarse-grained simulation.

3.3 Exploring the electronic structure of the solid oxide precursor material $LaCo_xFe_{1-x}O_3$ for $x \leq 0.5$

Dawn Geatches, STFC Daresbury Laboratory, Warrington WA4 4AD

Solid oxide fuel cells (SOFC) are an important class of energy conversion devices in the search to replace fossil fuels. Their electrodes' materials mostly belong to the perovskite family, which in their composition are versatile and numerous. For this study involving myself, Sebastian Metz (DL) and a couple of colleagues from Germany and the US specialising in experimental studies of SOFC, we focussed on the perovskite $LaCo_xFe_{1-x}O_3$.The aim of the theoretical study was to examine its electronic structure for $x \leq 0.5$ using density functional theory with a plane wave basis set and pseudopotentials, to provide information on the oxidation, spin states and magnitudes of Fe and Co throughout an increasing Co:Fe ratio.

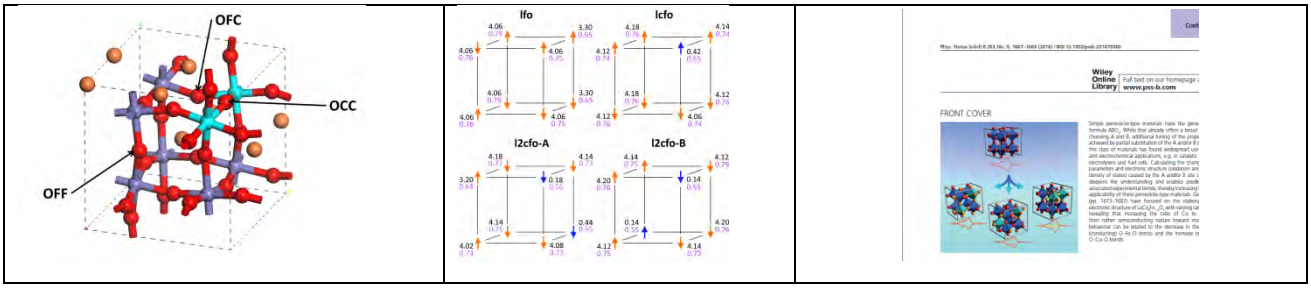

Figure 3.3.1: On the left is an example of a unit cell and the labels used to describe the different oxygen environments e.g. OFC describes O (red) between Fe (grey-blue) and Co (cyan). In the middle is an example of spin (black) and charge (purple) analysis for (clockwise from top left) $LaFeO_3$, $LaCo_{0.125}Fe_{0.875}O_3$, and two variations of $LaCo_{0.25}Fe_{0.75}O_3$, where the arrows indicate the direction of spin for Fe (orange) and Co (blue). On the right is a snapshot of the resulting article featured on the front cover of the September 2016 issue of Physica Status Solidi B.

The results showed the charge and spin magnitudes of oxygen ions is determined by their location; increasing the ratio of Co to Fe in oxygen stoichiometric materials decreases the relative, semi-conducting nature of the compounds towards insulating; Co-O, d-p hybridization is a necessary factor for the appearance of an intermediate spin state of Co. This research was published earlier this year[1], and we are continuing to work with our European partners on similar materials with the longer-term aim of applying for H2020 funding.

We used the electronic structure code CASTEP[2], 16.1.1 installed as the current version on SCARF and ran approximately 40 separate calculations, 32 of which used 64 cores. The longest calculation required over 130 hours to complete, and overall the maximum memory usage during the calculations was about 100 Gb. Electronic structure code calculations are particularly compute intensive, although this is ameliorated to some extent by the longer queue length and consequently longer running time. This allows the code sufficient time to write a checkpoint file from which the calculation can be re-started, thereby increasing overall compute efficiency.

References

[1] D Geatches, S Metz, D Mueller, and J Wilcox, Phys. Status Solidi B **253**, No. 9, 1667–1669 (2016)
[2] Clark, S.J., Segall, M.D., Pickard, C.J., Hasnip, P.J., Probert, M.J., Refson, K., and Payne, M.C. (2005) Castep v5.0. Zeitschrift für Kristallographie, 220, 567–570

3.4 Improving the fast electron collimation via grading the atomic number at resistive guide element transition region

R. A. B. Alraddadi, N. C. Woolsey, J. Pasley (University of York, York Plasma institute), A. P. L. Robinson (STFC Central Laser Facility, CLF)

Fast electron spreading is critical issue in the development of a number of high-intensity laser-plasma applications: fast electron driven ion accelerators and x-ray sources and warm dense matter studies. Experimental evidences indicated that the electron divergence angle is enormous at relativistic intensity of $I_L \lambda_L > 10^{18} W cm^{-2} \mu m^2$ [1,2]. Self-pinching of the fast electron beam, due to self-generated magnetic field, is not sufficient to collimate fast electron along the depth of the target [3].

The resistive guiding concept is promising technique to collimate these highly divergent electrons [4,5]. Once a high-Z guide material embedded in a lower-Z substrate, a resistivity gradient is created by a transition between two materials. This enables the growth of a strong resistive magnetic field according to induction equation in the hybrid approximation. Hence, the transverse fast electrons confined over a certain distance along the guide.

We used SCARF-MagnaCarta resources to run three-dimensional Hybrid-PIC code, namely ZEPHYROS, to investigate the effect of grading the atomic number at resistive guide element transition region. This creates linear gradient in resistivity rather than step-like gradient at the transition region. The newly design shown in Figure 1 (d) and numerically compared with other guide designs that shown in Figures 3.4.1 (a) to (c).

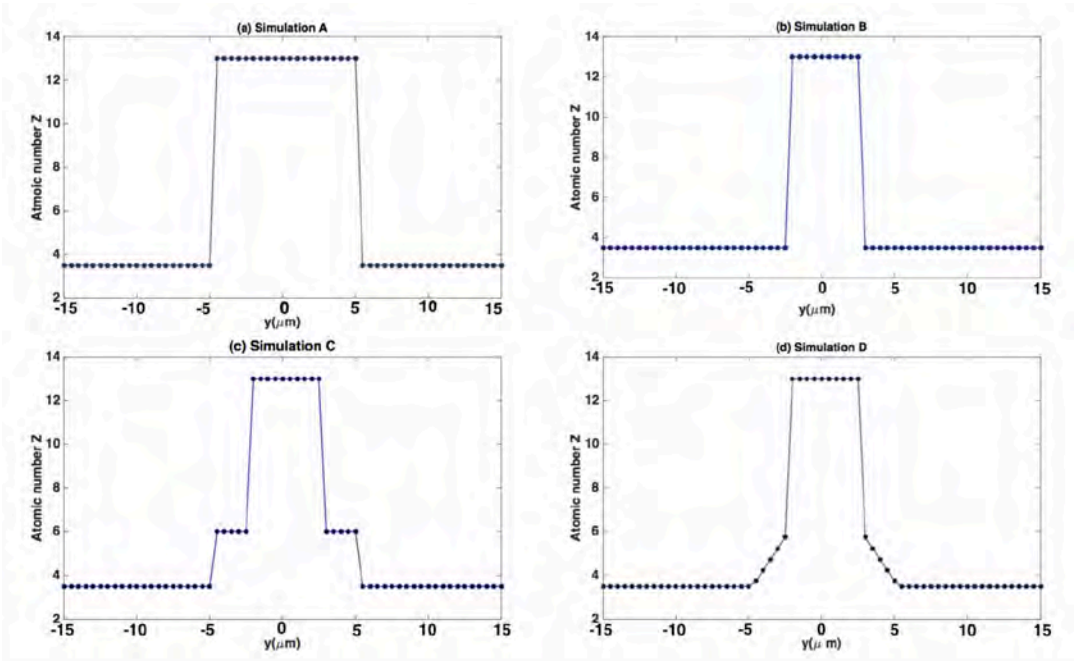

Figure 3.4.1: The radial atomic number profile for simulations A to D, respectively. Simulations A and B use Aluminum guide. Simulation C uses an Al guide clad in a carbon layer. Simulation D uses an Al guide clad in a graded layer of the material of linearly decreasing Z. All the guides are embedded into the CH plastic substrate.

We find that grading the atomic number at the transition region (simulation D in Figure 3.4.1) enhances the growth of resistive magnetic field, leading to a large integrated product of magnetic flux density and its width as shown in Figure 3.4.2. This results in significant improvements in both magnetic collimation and fast-electron temperature uniformity across the guiding.

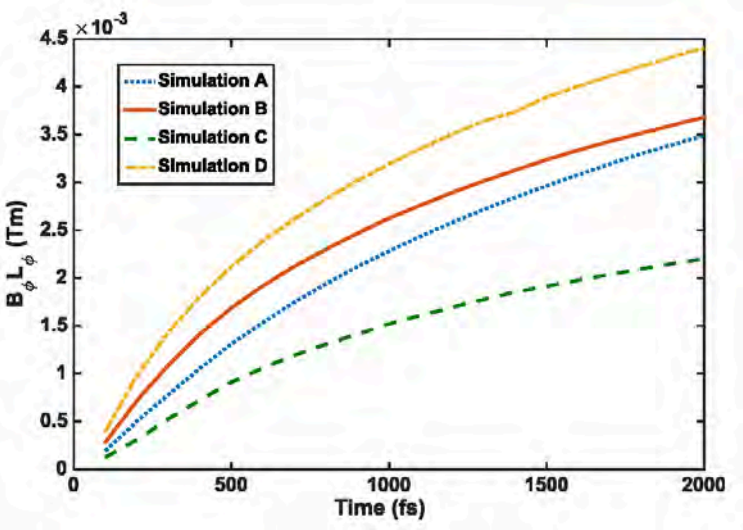

Figure 3.4.2: The product of integrated magnetic flux density and its width near the head of the beam at different times in fs.

References

[1] K. L. Lancaster et al., *Phys. Rev. Lett.*, 98(2007)125002.

[2] J. S. Green et al., *Phys. Rev. Lett.*, 100(2008), 015003.

[3] A. R. Bell and R. J. Kingham, *Phys. Rev. Lett.*, 91(2003), 035003.

[4] A. P. L. Robinson and M. Sherlock, *Phys. Plasmas*,14 (2007)083105.

[5] A. P. L. Robinson et al, Phys. Plasmas, 20(2013)122701.

3.5 Charge Transfer Processes in Combretastatins: A TDDFT Study of potential Cancer Drugs

Nicole Holzmann[1], Leonardo Bernasconi[1], Roger H. Bisby[2], Anthony W. Parker[1]

1. STFC Rutherford Appleton Laboratory, Harwell Oxford, Didcot OX11 0QX, UK
2. School of Environment and Life Sciences, University of Salford, Salford M5 4WT, UK

First isolated in 1982 from bark of African bush willow by Pettit[1], combretastatins are promising anti-cancer drugs targeting microtubule assembly. While the naturally occurring *cis* (Z-) isomers of those stilbene-based compounds show high cytotoxicity, their *trans* (E-) analogues are considerably less toxic. Photoisomerisation from the *trans* to the *cis* isomers can be achieved by both one- and two-photon excitation, the latter enabling the use of tissue penetrating wavelengths in the red or near-infrared region[2].

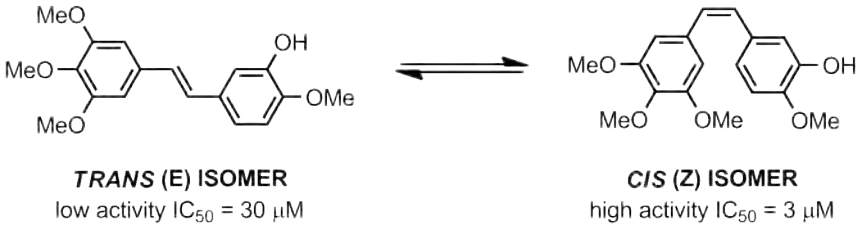

Figure 3.5.1: Light induced *trans-cis* isomerisation in combretastatins

Substitutions of functional groups by electron pushing and electron pulling moieties have been conducted to introduce a charge transfer character in these compounds. This results in significant changes in the spectroscopic properties: in particular fluorescence spectra exhibit enhanced red shifts with respect to non-charge transfer combretastatins or their sensitivity in solvents of increasing polarity. An increase in the two-photon absorption cross section has also been observed, which suggests that charge transfer combretastatins are potential drug molecules for *in-vivo* two-photon isomerisations[3].

In order to analyse the charge transfer effect in different stilbene derivatives on the optical spectra the *trans* isomers in Figure 3.5.2 (left) with low (non-CT1 and non-CT2) and high (CT1 and CT2) charge transfer character were considered for computational study. On SCARF, we performed geometry optimisations of the ground state molecules using NWChem6.6[4]. For excited states calculations and spectra determination the TDDFT method was applied considering the 50 lowest excited states.

In accordance with experiment (for non-CT1, non-CT2 and CT1) we calculated absorption and fluorescence spectra that are significantly red shifted for the charge transfer combretastatins compared with their non-charge transfer analogues (Figure 3.5.2, right).

The most prominent peak in the spectra of all derivatives corresponds to the first singlet excited state resulting from an excitation of one electron from the HOMO into the LUMO (for CT1 in Figure 2, middle). This excitation from a C=C π bonding orbital into an π anti-bonding orbital leads to a loss in C=C double bond character thus facilitates the rotation around this bond that leads to isomerisation. Another indication for the loss of double bond character is the increased C=C bond length in the excited state of the combretastatins with respect to their ground state structure while the C-C_{ar} single bond lengths shorten. In accord with the bond length behavior the planarity of the

C_{ar}-C=C-C_{ar} moiety is sacrificed as the dihedral angle decreases slightly from 180° by 0.9 for CT1 and 2.0° for non-CT1 and non-CT2.

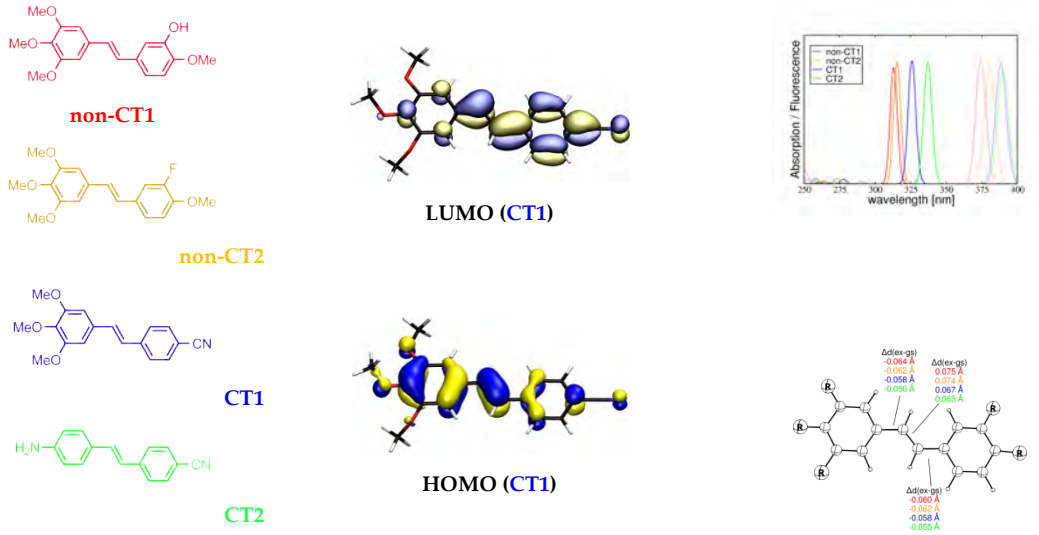

Figure 3.5.2: Stilbene derivatives of different charge transfer character (left), frontier orbitals of CT1 (middle), calculated absorption and fluorescence spectra and bond length differences of ground and excited state (right)

However, all these structure changes appear to be more pronounced in the non-CT compounds. This indicates that more C=C double bond character is conserved in the charge transfer derivatives which might hinder the C=C bond rotation required for isomerisation. If the reaction barrier to reach the isomerisation potential well on the excited state surface is higher for compounds with larger charge transfer character this might diminish or cancel the benefits we gain by increased excitation wavelengths or cross sections. In order to shed more light on how the excited state potential energy surface and thus the isomerisation is influenced by the charge transfer character of the stilbene derivatives we plan to carry out further calculations on SCARF: In a first step we will investigate the excitation of the *cis* isomer. Based on the so gathered information we plan to then perform excited state dynamics to assess the missing points on the potential energy surfaces.

References

[1] Pettit, G. R., Cragg, G. M., Herald, D. L., Schmidt, J. M., Lohavanijaya, P. *Can. J. Chem.* **1982**, *60*, 1374.

[2] Scherer, K. M., Bisby, R. H., Botchway, S. W., Hadfield, J. A., Parker, A. W. *J. Biomed. Opt*. **2015**, *20*, 051004.

[3] Scherer, K. M., Bisby, R. H., Botchway, S. W., Greetham, G. M., Hadfield, J. A., Parker, A. W., Towrie, M. *Biomed. Spectrosc. Imaging*, **2014**, *3*, 211.

[4] Valiev, M., Bylaska, E. J., Govind, N.; Kowalski, K., Straatsma, T. P., Van Dam, H. J. et al. *Computer Physics Communications*, **2010**, *181*, 1477.

3.6 Stabilization of 3d-transition metal hydrido complexes in $SrH_2Mg_2[Co(I)H_5]$, $BaH_2Mg_5[Co(-I)H_4]_2$ and $RbH_2Mg_5[Co(-I)H_4$ $Ni(0)H_4]$ *via* easily polarizable hydride ligands

Henrik Fahlquist,[1] David Moser,[1] Dag Noréus,[1] Keith Refson[2,3] and Stewart F. Parker[3]

1. Department of Materials and Environmental Chemistry, Arrhenius Laboratory, Stockholm University, S-106 91 Stockholm, Sweden
2. Department of Physics, Royal Holloway, University of London, Egham TW20 0EX, UK
3. ISIS Facility, STFC Rutherford Appleton Laboratory, Chilton, Didcot, OX11 0QX, UK

The purpose of the present paper was to investigate how 18 electron hydrogen complexes based on $Mg_2[CoH_5]$ [1,2] reacted to substitution of the strongly polarizing Mg^{2+} ions with softer and less polarizing counterions. A low formal oxidation state in a $[Co(-I)H_4]^{5-}$ complex could be stabilized in $BaH_2Mg_5[Co(-I)H_4]_2$ with the use of the more electropositive and less polarizing Ba^{2+} ion. By further substituting the Ba^{2+} ions with Rb^{+} ions, the structure can essentially be retained in $RbH_2Mg_5[Co(-I)H_4][Ni(0)H_4]$ if a corresponding number of $[Co(-I)H_4]^{5-}$ complexes are substituted by $[Ni(0)H_4]^{4-}$ complexes. This indicates the importance of the electron count for forming these hydrides. In $SrH_2Mg_2[Co(I)H_5]$ the higher formal oxidation state of + I for cobalt is maintained, when Mg^{2+} is partly substituted by Sr^{2+}, which is not as soft as Ba^{2+} and Rb^{+}. The resulting electron dense complexes are hydrogen rich with interesting electron conductivity properties related to how the lattice helps to relieve the high electron density in the complexes [3].

CASTEP calculations on SCARF were used to study the electronic structure and to assign the neutron vibrational (INS) spectra. Figure 1 shows the electronic density of states ($g(\varepsilon)$) for $BaH_2Mg_5[Co(-I)H_4]_2$ and $SrH_2Mg_2[Co(I)H_5]$. The partial density of states clearly shows different crystal field splitting of the 3d orbitals for the Ba (tetrahedral Co) and Sr (square-based pyramidal) hydrides, with the lower energy part of the 3d orbital manifold overlapping with the hydrogen 1s orbitals in a bonding interaction. For $SrH_2Mg_2[CoH_5]$, the Co 3d orbitals account for most of the total density of states between −3 and 0 eV. For $BaH_2Mg_5[Co(-I)H_4]_2$, this is not the case, and there is significant overlap with the Mg orbitals, consistent with a degree of covalent bonding between Mg and Co. The difference between the Sr and Ba hydrides is probably because the closest M-to-Co distance is 2.686 Å for M = Sr, but 2.430 Å for M = Ba.

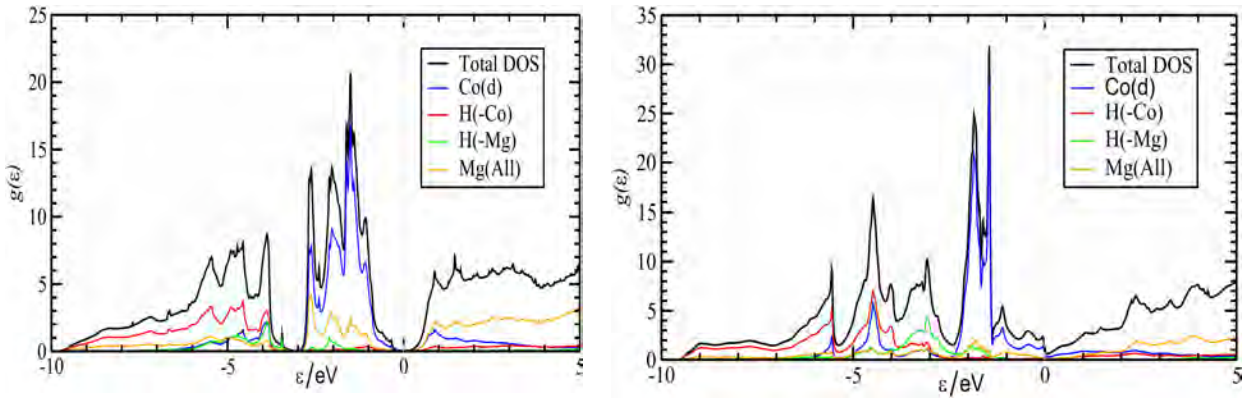

Figure 3.6.1: Electronic density of states ($g(\varepsilon)$) (black) of: (left) $BaH_2Mg_5[Co(-I)H_4]_2$ and (right) $SrH_2Mg_2[Co(I)H_5]$. The partial density of states for the cobalt d-orbitals (blue) and the hydrogen atoms bonded to the cobalt (red) and the interstitial hydrogens (green) are also shown.

The INS spectra of $BaH_2Mg_5[Co(-I)H_4]_2$ and $SrH_2Mg_2[Co(I)H_5]$ are shown at the top of Figures 2a and 2b, respectively. The spectra can be summarized as M−H stretching modes 1600−1900 cm^{-1}, H−M−H bending modes and H− translations 700−1200 cm^{-1}, complex ion librational modes 350− 700 cm^{-1} and heavy atom translation modes (acoustic and optic) 0−350 cm^{-1}. To go beyond this simple description, additional information is required which can be obtained from the CASTEP ab initio calculations. The CASTEP calculations show that there is significant variation in transition energy with wavevector (dispersion) in the modes as shown by the dispersion curves.

Since the INS spectrum is purely dynamic, we can investigate the contributions of the individual species separately. By setting the cross-section of all the atoms to zero, except for the atoms of interest, only the modes involving motion of those atoms will contribute to the calculated INS spectrum, as depicted in Figures 2a and 2b. The "spectra" largely confirm the qualitative expectations but also show that the interstitial hydrogen atoms exhibit relatively pure modes at 600−750 and 900−1000 cm^{-1} and account for most of the intensity in this region. The translational modes of the magnesium ions are all at <450 cm^{-1} with those of the barium ion largely below 200 cm^{-1}. As expected, below 450 cm^{-1} there is significant mixing of modes and there are no pure modes.

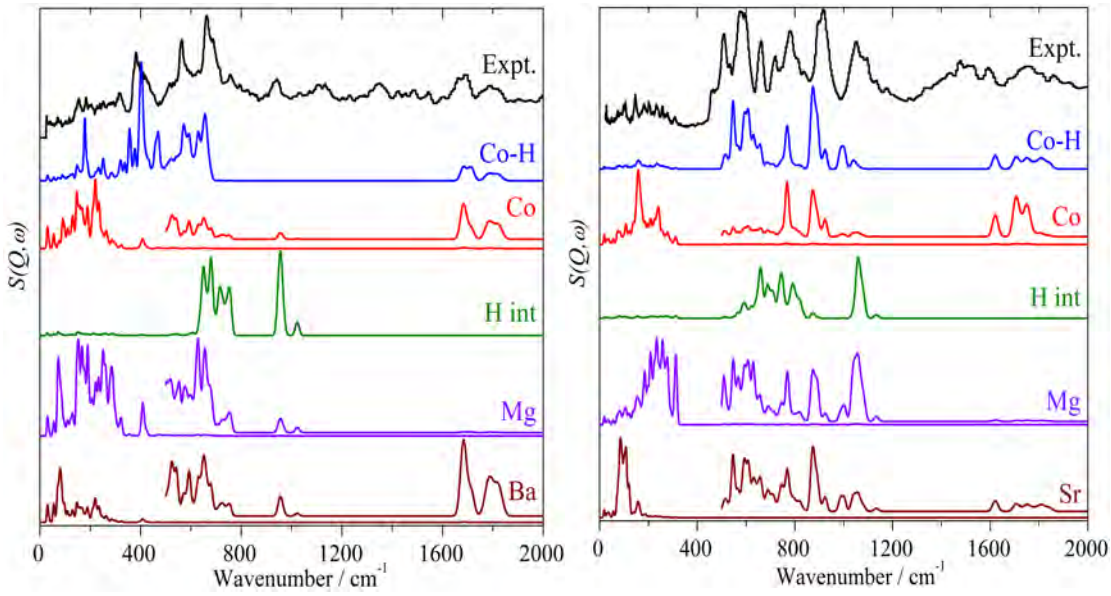

Figure 3.6.2: (Comparison of the experimental (expt, black) INS spectrum of (left) $BaH_2Mg_5[Co(-I)H_4]_2$ and (right) $SrH_2Mg_2[Co(I)H_5]$. with those generated by including only the motions of the hydrides bonded to the cobalt (Co−H, blue), the cobalt atoms (Co, red), the interstitial hydrides (H int, olive), the magnesium ions (Mg, violet), and the barium (Ba) or strontium ions (Sr) (brown), only the 0 → 1 transitions are shown.

References

[1] Zolliker, P.; Yvon, K.; Fischer, P.; Schefer, J. *Inorg. Chem.* **1985**, *24*, 4177−4180..
[2] Parker, S. F.; Jayasooriya, U. A.; Sprunt, J. C.; Bortz, M.; Yvon, K. *J. Chem. Soc., Faraday Trans.* **1998**, *94*, 2595−2599.
[3] Fahlquist, H.; Moser, D.; Noréus, D.; Refson, K.; Parker, S.F. *Inorg. Chem.* **2016**, *55*, 3576-3582.

3.7 DFT simulation of icy planetary materials

Dominic Fortes (ISIS Crystallography)

DFT calculations done using CASTEP on the SCARF cluster have been used to support and direct a program of experimental studies into 'rock forming' minerals present in the outer solar system. Primarily this consists of a range of divalent metal sulfate hydrates with high water to cation ratios. These materials are relevant to understanding the interiors of icy bodies: since they are likely to be precipitated during secular cooling of the vast subsurface brine oceans we know to be present inside the largest icy moons, then the associated volume and enthalpy changes have implications for their overall structure and thermal evolution. Additionally, they are of intrinsic interest by virtue of their complex high-pressure behaviour – involving progressive exsolution of ice to form novel hydrates – and also the presence of extended polymeric water clusters in their structures.

Work has been done on the newly-discovered metastable hydrate, $MgSO_4{\cdot}9H_2O$ ($P2_1/c$, Z = 4), which is formed experimentally only by rapid immersion of aqueous $MgSO_4$ droplets in liquid nitrogen. Calculations were done in order to determine the energetic stability of this phase with respect to another candidate structure, based on that of $MgSeO_4{\cdot}9H_2O$ [1] and to characterise the elastic properties of $MgSO_4{\cdot}9H_2O$. This involved calculating the complete elastic stiffness tensor of the material. A paper describing this work is currently in review with *Acta Cryst. B*.

In related work, calculations have been carried out on two new metastable hydrates of nickel sulfate, $NiSO_4{\cdot}9H_2O$ (isotypic with the Mg-analogue) and $NiSO_4{\cdot}8H_2O$ ($P\bar{1}$, Z = 2). The major contribution made by the calculations was in evaluating the spin coupling between Ni ions and characterising the solid solution series between Mg and Ni end-members of the enneahydrates. A paper describing this work will be submitted to *Physics and Chemistry of Minerals* in early 2017.

Similarly, CASTEP calculations have been used to study the site preferences of Co^{2+} and Mn^{2+} in the structure of meridianiite, $MgSO_4{\cdot}11H_2O$ ($P\bar{1}$, Z = 2). It is known from prior work that these two cations are able to readily substitute for Mg^{2+} [2,3], and I have done extensive equilibrium crystallisation studies to determine the solid-liquid distribution coefficients. Part of this used single-crystal neutron diffraction measurements, which revealed an unexpected difference in preference for the 1*a* and 1*b* octahedral sites between cobalt and manganese. DFT calculations helped to understand these observations (Figure 3.7.1) and a paper was recently submitted to *Fluid Phase Equilibria*.

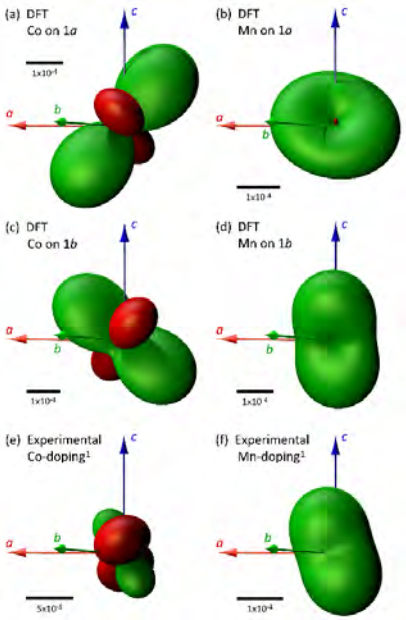

Figure 3.7.1: Figure 1: DFT calculated unit-strain tensor representation surfaces reflecting the change in unit-cell parameters of meridianiite when either Co^{2+} or Mn^{2+} are doped entirely on the 1*a* or 1*b* sites. The two strain figures at the bottom show the experimental observations.

Other work in progress includes: (*i*) a complete set of consistent geometry optimizations, E-field calculations and partial Raman spectrum calculations for all known $MgSO_4$ hydrates; (*ii*) calculation

of the equation of state of a sodium magnesium sulfate hydrate, blödite; (*iii*) simulation of negative linear compressibility in methanol monohydrate [*cf*., 4]; and (*iv*) DFT calculations on various framework materials to support ISIS experiments, including the Al_2SiO_5 polymorphs (kyanite, andalusite, sillimanite), $NaBePO_4$ (beryllonite) and the ceramic Na_2MoO_4.

References

[1] Fortes *et al.* (2015) *Acta Cryst. B* **71**(3), 313–327.

[2] Fortes *et al.* (2012) *Phys. Chem. Min*. **39**(6), 443–454.

[3] Fortes *et al.* (2012) *Phys. Chem. Min*. **39**(5), 419–441.

[4] Fortes *et al.* (2011) *Science* **331**, 742–746

3.8 Vibrational motions in the low-temperature phases of CBr_nCl_{4-n} (n=0,1,2) from Inelastic Neutron Scattering and Density-functional Theory

Oriol Abril Pla,[1] Daniel Moreno García,[1] Sanghamitra Mukhopadhyay,[2,3] Luis Carlos Pardo,[1] Josep Lluís Tamarit,[1] and Felix Fernandez-Alonso[2,4]

1. Grup de Caracterització de Materials, Departament de Física, Universitat Politècnica de Catalunya
2. ISIS Facility, Rutherford Appleton Laboratory, Chilton, Didcot, Oxfordshire OX11 0QX
3. Department Of Materials, Imperial College London, Exhibition Road, London SW7 2AZ
4. Department Of Physics And Astronomy, University College London, London WC1E 6BT

By cooling the room temperature liquids formed by tetrahedral molecules of formula CBr_nCl_{4-n}, n = 0, 1, 2, leads to rotationally disordered crystalline phases which show translational face-centered cubic or rhombohedral lattices with the center of mass of molecules sitting at the lattice nodes. Further cooling leads to a transformation into complex monoclinic, C2/c structures with Z = 32 molecules per unit cell and an asymmetric unit with Z ′ = 4. Molecular motions within such C2/c crystals persist down to ≈90 K where a calorimetric transition much alike that exhibited by the canonical glass-transition. Results derived from the concurrent use of NQR and molecular simulations show that large-angle rotations of tetrahedral about their higher symmetry axes (CCl_3Br, and CCl_2Br_2 with C_{3v} and C_{2v} point-group symmetries, respectively) lead to a statistical occupancy of 75% for Cl and 25% for Br atoms in the case of CCl_3Br, and 50% for Cl and 50% for Br atoms for CCl_2Br_2. To understand the vibrational dynamics at molecular and lattice levels, INS experiments on the TOSCA spectrometer at ISIS and DFT first principles simulations using the CASTEP code were performed.

Ab-initio calculations using different functionals and pseudopotentials were able to describe the experimental results. In particular, the GGA approximation gives the best results and, in that case, dispersion corrections give no significant improvement.
In the particular case of CCl_4, calculations were not able to reproduce the experimental results unless the presence of ^{35}Cl and ^{37}Cl is taken into account explicitly. Calculations for several isotopic combinations show that the "natural abundance", i.e., $C^{37}Cl^{35}Cl_3$, provides the best match to the experimental data.

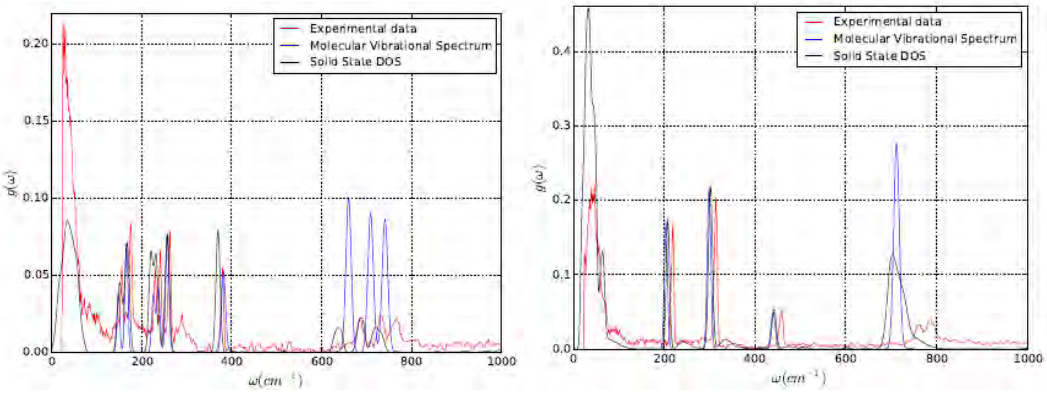

Figure 3.8.1: Experimental (red) and calculated density of states (black) and vibrational spectrum for CCl_2Br_2 (Left Panel) and CCl_4 (Right Panel).

3.9 CCP5 flagship: Coarse Grain modelling – the case of DOPC lipids

Andrey Brukhno[1] and Stephen Parker[2]

1. Computational Chemistry, SCD, STFC, Daresbury Laboratory, UK
2. Department of Chemistry, University of Bath, UK

An important challenge, particularly faced by the soft matter community, is to understand and predict the phase behaviour and stability for systems where the numbers of atoms required are too large for atomistic MD and/or suffer from the time constraints of observing slowly evolving processes. One method to overcome this for complicated molecular structures such as polymers, liquid crystals and biomolecules is to reduce the number of degrees of freedom by using coarse grained (CG) models in which several atoms are grouped into effective interaction sites (CG sites or "beads"). Thereby a vast amount of 'uninteresting' local scale patterns of motion (with relatively short relaxation times), are excluded from consideration. This makes simulation of a CG system significantly less resource and time demanding. The principal problem, however, remains: how to efficiently devise and optimise a reliable and thermodynamically transferrable CG model?

This project aims at developing a general simulation protocol for density/concentration independent coarse graining (CG) to model complex molecules. As a case study, DOPC lipid molecules and their aggregates are considered. The protocol is especially suited for developing “solvent-free” CG models, by removing from the CG representation small solvent species, such as water. It renders itself reliable in the case of two-tail lipid molecules, such as DOPC, resulting in the derived CG model(s) that reproduce a stable bilayer system, and its properties known from atomistic MD simulation and experiment.

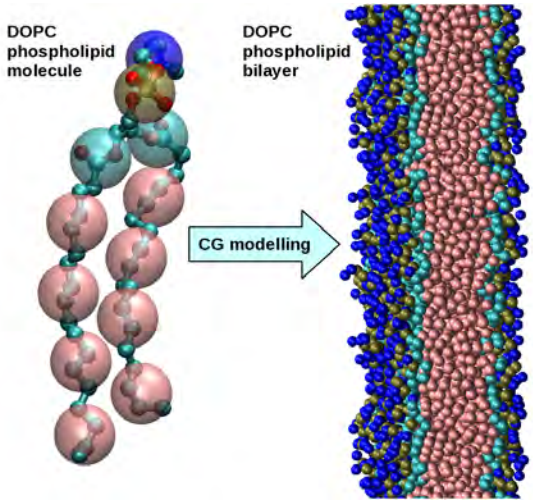

The simulations performed on Scarf included both (i) obtaining sufficient statistics for reference full-atom systems, including free energy and CG probability distributions for two and many molecule systems; and (ii) self-consistent optimization of CG models within the suggested protocol using VOTCA and/or DL_CGMAP software, which is a tedious and demanding task requiring dozens of iteration cycles.

This work is followed by an analogous study in the case of surfactants.

3.10 Discovering connections between Terahertz vibrations and elasticity underpinning the collective dynamics of the HKUST-1 metal-organic framework

Matthew R. Ryder,[1,2] Bartolomeo Civalleri,[3] Gianfelice Cinque[2] and Jin-Chong Tan[1]

1. Department of Engineering Science, University of Oxford
2. Diamond Light Source, Harwell Campus
3. Department of Chemistry, University of Turin

Metal-organic frameworks (MOFs) are contemporary nanoporous solids with vast structural versatility, giving rise to highly tuneable physical and chemical functionalities. The current trend is rapidly shifting from purely chemical structure discovery to development of potential applications to afford commercial use in industry, engineering, and value-added products. In fact, research into potential applications of MOFs is no longer limited to gas separations, carbon capture and adsorption, but expanding into many innovative domains encompassing optoelectronics and lighting, biomedicine, heterogeneous catalysis and chemical sensing.

We employed a combination of theoretical and experimental techniques to study the MOF-mechanics central to the paddle-wheel $Cu_3(BTC)_2$ porous structure, commonly designated as HKUST 1. Lattice dynamics of the hybrid framework at below 18 THz were measured by means of Raman and synchrotron far-infrared spectroscopy, and systematically correlated to collective vibrational modes computed from *ab initio* density functional theory (DFT). We identified a number of intriguing low-energy framework vibration mechanisms, reminiscent of the 'trampoline-like' deformations and new oscillatory motions associated with Cu paddle-wheel 'molecular rotors'. The three independent single-crystal elastic constants of the HKUST 1 (i.e. C_{11}, C_{12} and C_{44}) were calculated using the DFT approach, taking into account the effects of dispersion corrections. We established the full elasticity solutions accompanying detailed deformation mechanisms that control its anisotropic mechanical properties, ranging from the Young's and shear moduli to linear compressibility and Poisson's ratio. Our results support the notion that the co-existence of soft modes and intrinsic shear distortions connected to the THz lattice dynamics dictate a range of anomalous elastic phenomena, for exemplar: negative Poisson's ratio (auxeticity), negative thermal expansion (NTE), and exceedingly low shear moduli properties.

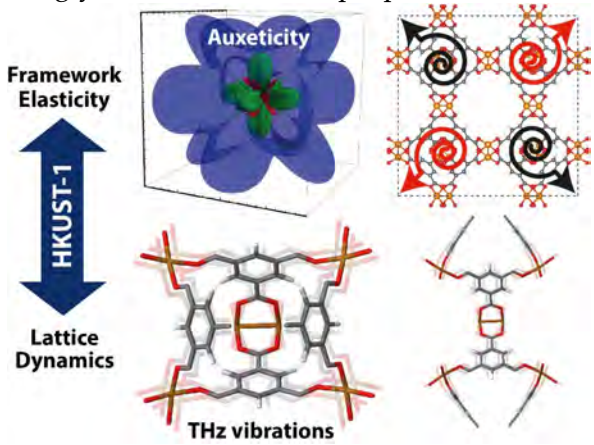

Figure 3.10.1: Framework elasticity and lattice dynamics of HKUST-1.

References

[1] M. R. Ryder *et al.*, *CrystEngComm*, **18**, 4303 (2016).

3.11 FLUKA dose rate distribution maps

Xavier Queralt Compte, ISIS

During 2016, I have used SCARF to do some shielding calculations using flair/FLUKA package. I used the results from these output on 2 internal documents:
1. Dose rate calculations for the transportation ISIS-RAL casket: TS1 target case - ONR ISIS-RAL Visit - Feb 2016
2. Dose rate calculation on the package 2917A surface using FLUKA code - ISIS/HOPI/010-4

These documents have been part of all the needed documentation to get the transport license from ONR (Office for Nuclear Regulation) for the target flask.
Here is shown the dose rate maps for the Co56 nuclide using the extended source (cylindrical geometry) located in the middle of the package (a) and the point source case, located at the top (b) and bottom (c) as it is indicated in Figure 4.

The statistical error distribution is given next to the dose rate maps, as it is expected the higher statistical errors are located outside the package where the dose rates are lower.

All package volume – Extended Source approach

In this case the highest dose rate is achieved towards the side direction at the source height and it is about an order of magnitude if we compare with the top and bottom directions. Although the source is closer to the bottom side, the dose rate at the top side is higher than at the bottom, this could be caused by the lead thickness difference in both directions. However, in the real case, we have to consider the thickness of the stainless steel from the target support.

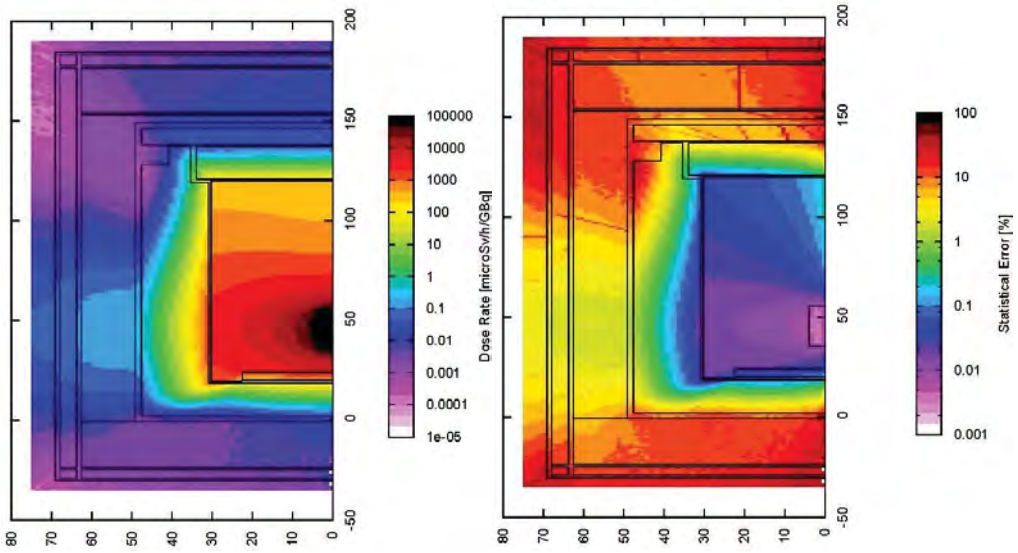

Top package volume – Point Source approach

The dose rates at the side and the top directions are very similar in this situation. This means that the dose rates are mainly driven by the lead thickness and not by the plug shape effect. This effect can be compensated by the liner attenuation that has not been considered on these FLUKA calculations.

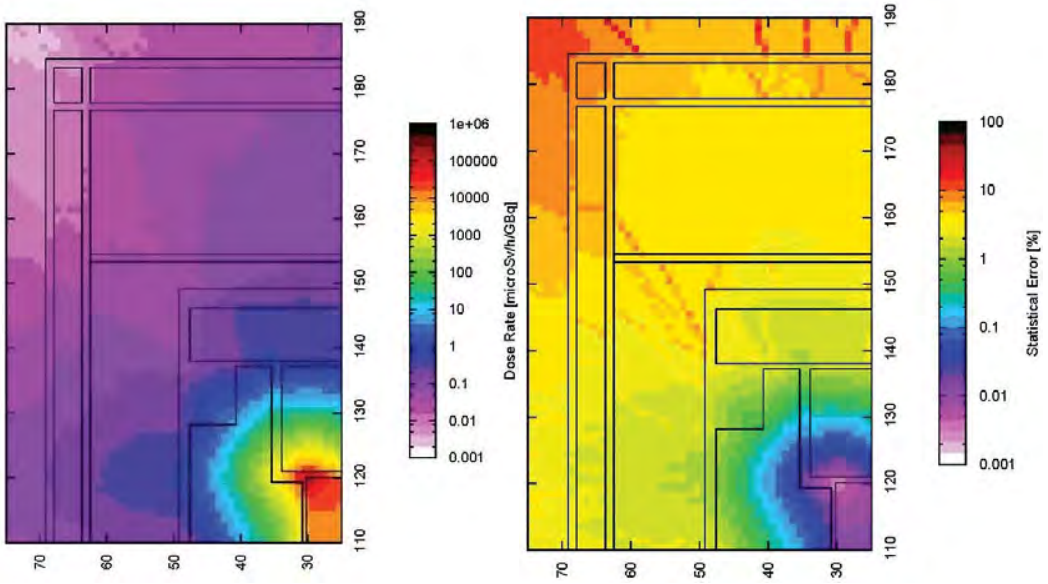

Bottom package volume – Point Source approach

If we compare this result with the previous one, one can observe that the dose rate is an order of magnitude lower in this case (in both directions side and bottom). The main reason could be that the plug shape interface on the top direction reduces the shielding effectiveness.

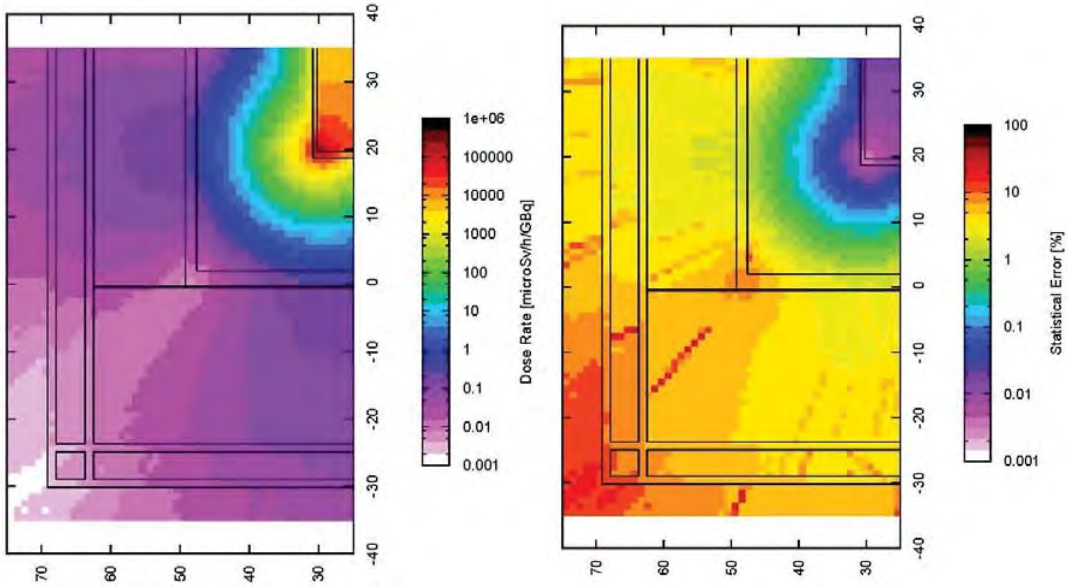

3.12 Dissipation mechanisms in gyrokinetic plasma turbulence

J. T. Parker, [1] E. G. Highcock, [2] A. A. Schekochihin, [3,4] and P. J. Dellar [5]

1. Science and Technology Facilities Council, Rutherford Appleton Laboratory, Harwell Campus, Didcot OX11 0QX, UK
2. Department of Physics, Chalmers University of Technology, SE-412 96 Go¨teborg, Sweden
3. Rudolf Peierls Centre for Theoretical Physics, University of Oxford, 1 Keble Road, Oxford OX1 3NP, UK
4. Merton College, Merton Street, Oxford OX1 4JD, UK
5. OCIAM, Mathematical Institute, University of Oxford, Andrew Wiles Building, Radcliffe Observatory Quarter, Woodstock Road, Oxford OX2 6GG, UK (Dated: November 6, 2016)

A longstanding question in fundamental plasma physics is the mechanism for dissipation of free energy. Energy in three-dimensional purely hydrodynamic turbulence is dissipated through a nonlinear forward cascade to fine spatial scales, where it eventually encounters viscous dissipation. By contrast, free energy, or disturbance amplitudes, in a one-plus-one dimensional plasma are dissipated through a linear transfer to fine scales in parallel velocity space through phase mixing, until eventually dissipated by collisions. The latter is the mechanism that underlies Landau damping, a linear process that involves no change in the physical space scale. Both avenues for dissipation are open to a multidimensional fusion plasma, but it only now becoming understood which mechanism is preferred and how the mechanisms interact.

We have developed a fully spectral kinetic code SpectroGK [1] to study these mechanisms. SpectroGK uses a Fourier representation in physical space, and a Hermite–Hankel representation in velocity space. This makes it an ideal tool for studying free energy transfers, as the spectral discretization exactly preserves quadratic invariants. Free energy is thus exactly transferred between wavenumbers through resonant triad interactions without spurious creation or destruction through numerical error, so the discretization has a meaningful statistical mechanics of its own.

In recent work [2], we used SpectroGK to study the drift-kinetic regime, for which perpendicular lengthscales are much larger than the Larmor radius. We showed that phase space is divided into two regions: one where phase- mixing dominates, and one where the nonlinear cascade dominates. In the former region, the system behaves likes the linearized system with a shallow Hermite spectrum and dissipation at fine velocity space scales. In the latter region, however, the nonlinearity interferes with the phase-mixing by exciting a reverse transfer of free energy from small to large scales in velocity space. This cancels the forward transfer and results in no net free energy to fine velocity space scales in this region, and therefore no dissipation. Moreover, since most of the free energy in the system is contained in the nonlinear region, the majority of the free energy cascades nonlinearly to small physical scales comparable with the Larmor radius. Using this insight, we have derived the full spectrum of drift-kinetic turbulence [3] and verified these scalings numerically [1, 2].

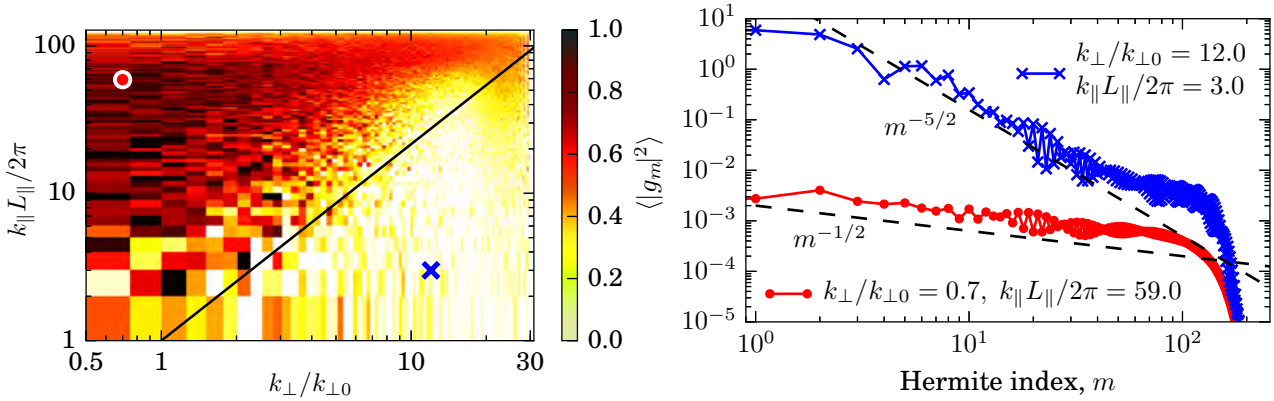

Figure 3.12.1: (a) Free energy transfer to fine velocity space scales in a drift-kinetic plasma, normalized to its value in the linearized system. The top left-hand region behaves like the linearized system, while the bottom right-hand region has almost no free energy transfer. (b) Hermite spectra expressing the free energy content at a fixed Fourier wavenumber and different parallel velocity space scales $\delta v_\parallel \sim 1/\sqrt{m}$. The two spectra correspond to the two regions in (a), and their positions in wavenumber space are marked on (a) with the corresponding symbol.

Since free energy cascades to lengthscales comparable to the Larmor radius, we are now using SCARF to investigate turbulence at these scales. Now "gyrokinetic" effects are important, as particles with different perpendicular velocities experience different electromagnetic fields during their gyration. This opens a new dissipation channel in perpendicular velocity space, in addition to the channels in parallel velocity space and perpendicular physical space which exist at larger physical scales. The gyrokinetic system is five-dimensional, with the extra perpendicular velocity space dimension, in addition to the four dimensions which appear in the drift-kinetic system. These simulations are particularly challenging because, in addition to the high dimensionality, we must also compute over a large range of physical scales to capture the transition from the drift-kinetic to the gyrokinetic regime. We will use these simulations to extend our scaling theory for four-dimensional drift-kinetic turbulence [3] to five-dimensional gyrokinetic turbulence.

References

[1] J. T. Parker. Gyrokinetic simulations of fusion plasmas using a spectral velocity space representation. DPhil Thesis, University of Oxford, arXiv:1603.04727, 2015.

[2] J. T. Parker, E. G. Highcock, A. A. Schekochihin, and P. J. Dellar. Suppression of phase mixing in drift-kinetic plasma turbulence. Physics of Plasmas, 23(7), 2016.

[3] A. A. Schekochihin, J. T. Parker, E. G. Highcock, P. J. Dellar, W. Dorland, and G. W. Hammett. Phase mixing versus nonlinear advection in drift-kinetic plasma turbulence. Journal of Plasma Physics, 82(2), 2016.

3.13 Processing of single-particle electron micrographs from the eBIC facility

Martyn Winn[1] and Paul Fyfe[2]

1. Scientific Computing Department, STFC
2. School of Life Sciences, University of Dundee

Recent advances in instrumentation and software have led to an explosion of interest in electron cryo-microscopy (cryoEM) for biological samples. In particular, the technique of single particle reconstruction allows the construction of models of macromolecular complexes, viruses or molecular machines at near-atomic resolution. In favourable cases, cryoEM now competes with macromolecular crystallography in providing structural information for biological systems.

Currently, eBIC (electron Bio-Imaging Centre) on the Harwell campus has two top-of-the-range Titan Krios electron microscopes, with users collecting data since June 2015. In a 48-hour allocation, 2 – 4 TB of raw data can be collected, and processing of this data is a major bottleneck. The MRC-funded CCP-EM project (www.ccpem.ac.uk) exists to provide computational support to the cryoEM community, including users of eBIC. We have been working closely with SCARF to develop a data processing facility for eBIC users.

The most popular software for single particle reconstruction is Relion, developed by Sjors Scheres at the MRC Laboratory of Molecular Biology in Cambridge. We installed Relion version 1.4 on SCARF and benchmarked its performance, see http://www.ccpem.ac.uk/user_help/relion_benchmarks.php. More recently, a beta version of SCARF v2.0 has been made available (see Figure 1), in which computationally-intensive routines have been GPU-enabled. This is now also installed on SCARF, with GPU-enabled modules compiled for EMERALD. We have also installed additional utilities required to prepare data for Relion, and John Kewley in SCD has installed the Scipion package (work for an EGI Competency Centre in structural biology).

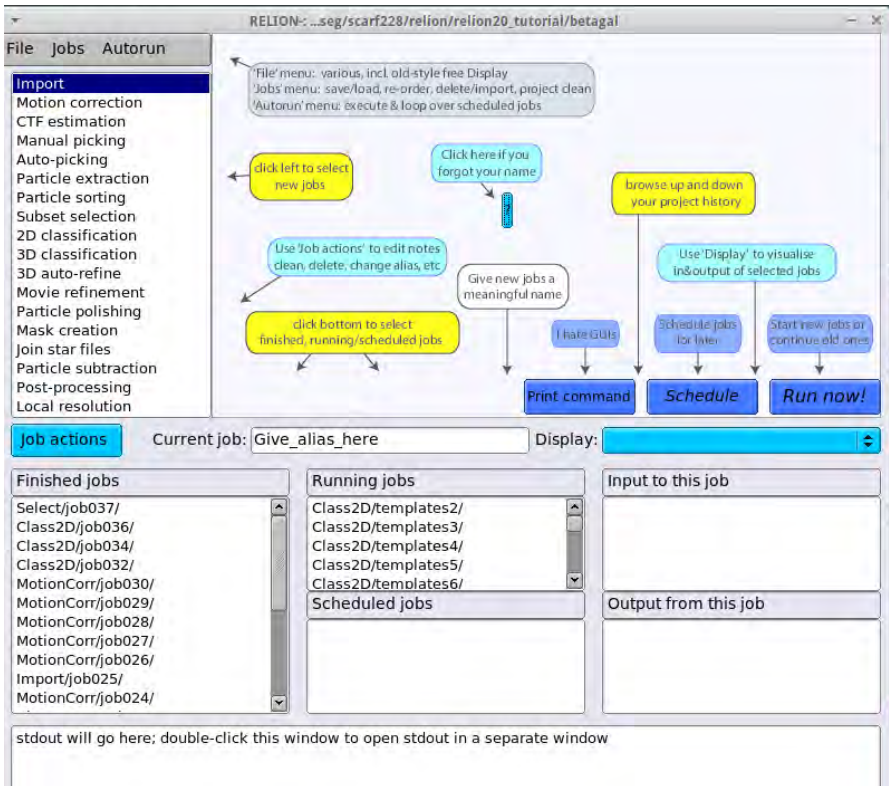

Figure 3.13.1: Relion 2.0 for cryoEM single particle reconstruction, installed on SCARF.

One of us (PF) has recently collected data at eBIC, consisting of 3300 micrograph movies and totalling 2.95 TB. This dataset was automatically copied to the ICAT tape storage at STFC within 1 week of data collection. From there, the dataset was copied to a new volume on the SCARF PaNaSaS storage dedicated to facility data. The data is now being processed, going through a pipeline involving creation of image stack files, motion correction, CTF estimation, particle picking, and creation of 2D class averages (see Figure 2). From around 320,000 particles picked, inspection and 2D classification suggests many false positives (empty micelles) which need to be removed. Once the set of particles is cleaned, the process of 3D reconstruction can begin. The process is lengthy, and still involves many manual steps, but is benefitting hugely from the processing power of SCARF.

3.14 TOSCA Neutron Spectrometer Primary and Secondary Upgrade

R.S. Pinna[1,2], M. Zanetti[1,2], S. Rudic[1], S.F. Parker[1], G. Gorini[2] and F. Fernandez-Alonso[1,3]

1. ISIS, Rutherford Appleton Laboratory, Harwell, UK
2. Università degli Studi di Milano-Bicocca, Milan, Italy
3. University College of London, London, UK

TOSCA is a high resolution indirect-geometry inelastic neutron spectrometer that can operate up to energy transfers of ca. 500 meV in neutron-energy loss. For TOSCA to move forward beyond the current state-of-the-art in key scientific areas such as gas and charge storage, the most urgent need is for greater sensitivity *via* provision of a guide in the primary spectrometer and the complete upgrade of the secondary instrument. Such an increase in incident flux implies an order-of-magnitude reduction in counting times by the neutron guide and up to a further order of magnitude gain by the secondary upgrade, a transformational development that would enable detailed studies of industrially relevant systems containing weak neutron scatterer or minute amounts of hydrogen, reducing the current limits up to two orders of magnitude [1, 2]. This extensive upgrade project would keep TOSCA competitive on a global scale for the foreseeable future.

During the past, our work has proceeded in the refinement of the TOSCA neutron guide (see previous SCARF reports for additional details), the benchmarking of the new MCNP-X moderator model and the development of the secondary spectrometer design by means of the McStas ray-tracing software. The needed simulations were performed on SCARF cluster, we used up to 128 cores and the typical duration was approximately 12 hours. Some of the latest calculations have been focused on the study of a new double-bent analyser which could substitute those currently installed in the TOSCA inelastic scattering modules. This innovative analyser will be capable to focus the scattered neutrons both on the horizontal and vertical direction, see Figure 3.14.1, in order to increase the solid angle coverage after the sample and thus dramatically improve the collection efficiency of the instrument. This kind of simulations requires high calculation power since the physical processes involved are manifold, i.e. moderations of the particles, scattering processes into the sample materials and Bragg diffraction onto the analyser. Another set of simulations was aimed at the study of the upgraded TOSCA beamline that is being installed at ISIS TS-1 and the new TOSCA water moderator model. The calculations confirm that the new moderator does not affect our previous conclusions about the neutron guide. In fact, the gains obtained with the implementation of the guided beamline are 50.9 ± 1.5 for the lowest incident neutron energy and 2.2 ± 0.2 for the highest one available on the instrument, thus confirming the design improvement predicted by Pinna (2014). At the elastic line, the gain is confirmed to be around 40 and 30 when the shutter guide is included and not, respectively.

We as well performed experiments on the TOSCA beamline in order to calibrate the simulation results and to validate the theoretical models used [3]. One of the exploited sample was Methylammonium Lead Iodide (MAPI) that has been highlighted as a possible calibration compound on TOSCA thanks to its narrow inelastic features and high scattering power, furthermore this material is also of high technological interest thanks to its cutting-edge application on solar cells; besides the measurement campaign performed on this material has unveiled some unexpected features at low temperatures that led to a publication [4].

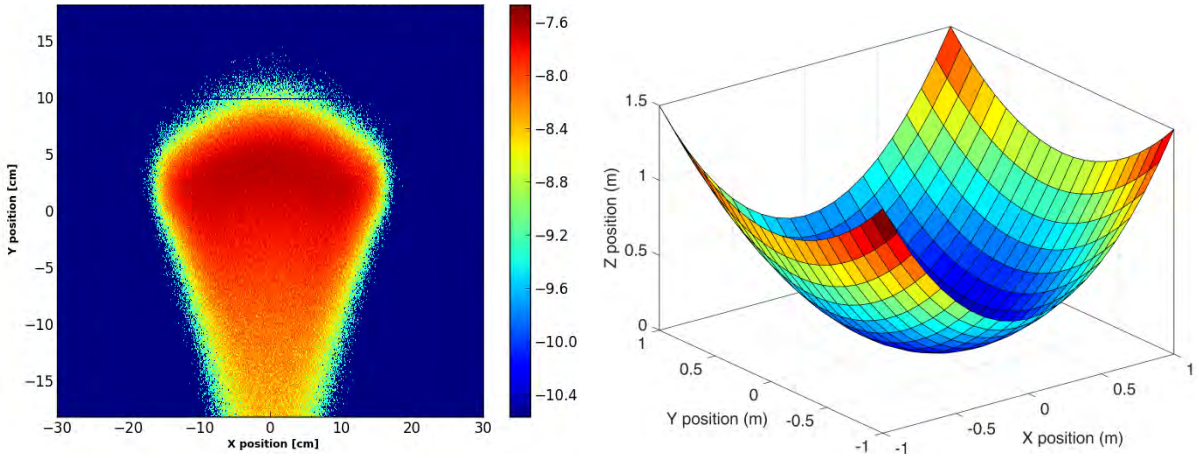

Figure 3.14.1: Monte Carlo ray-tracing simulations (left) of a TOSCA curved analyser (right) for the secondary upgrade project.

References

[1] Recent and future developments on TOSCA at ISIS, S. Parker, F. Fernandez-Alonso, A. Ramirez-Cuesta, J. Tomkinson, S. Rudic, R. Pinna, G. Gorini, and J. Castañon. Journal of Physics: Conference Series, 2014.

[2] Monte Carlo simulations of the TOSCA spectrometer: Assessment of current performance and future upgrades, R. Pinna, S. Rudic, S. Parker, G. Gorini, and F. Fernandez-Alonso. EPJ Web of Conferences, 2015.

[3] Neutron beam profile characterization on TOSCA, R. Pinna, S. Parker, M. Capstick, D. McPhail, D. Pooley, G. Howells, G. Gorini, F. Fernandez-Alonso, and S. Rudic, in preparation.

[4] Unexpected Cation Dynamics in the Low-temperature Phase of Methylammonium Lead Iodide – The Need for Improved Models, K. Drużbicki, R. Pinna, S. Rudic, M. Jura, G. Gorini, and F. Fernandez-Alonso, 2016. Submitted to the Journal of Physical Chemistry Letters. DOI: 10.1021/acs.jpclett.6b01822.

3.15 Changes to the structure of 1 M tetrapropylammonium bromide in acetonitrile solution on confinement in porous carbons

E. Humphreys, Cambridge University

Confinement of fluids in porous matrices can have a pronounced effect on their structural and dynamical properties. Any significant changes can have important consequences for applications that use such confined fluids. The effect of confinement in the porous space of activated carbon on the structure of 1 M tetrapropylammonium bromide in acetonitrile solution (TPA-Br in acn) has been examined experimentally using neutron total scattering (on NIMROD at ISIS). Empirical potential structure refinement modelling work has also been carried out using SCARF to examine the effect of different carbon pore geometries when confining TPA-Br in acn.

The calculations performed on SCARF allowed the degree of ion association in the different confinement geometries to be probed, as well as the allowing the three dimensional spatial density distribution functions of the different solution species to be examined. The results showed that the size of the confining space is one of the key factors determining the magnitude of any structural changes, with large pore spaces having a very limited effect on the confined solution structure (as illustrated in Figure 1). Furthermore, the results also suggested that the geometry can have a significant effect on the solution structure due to different space restrictions. One particular geometry (creating using graphene fragments) completely disrupted the ion-ion interactions and caused significant changes in the ion-solvent structure, as shown in Figure 2. The degree of ion association seemed to be predominantly effected by the size of the confining space. The work formed part of the PhD project of Elizabeth Humphreys.

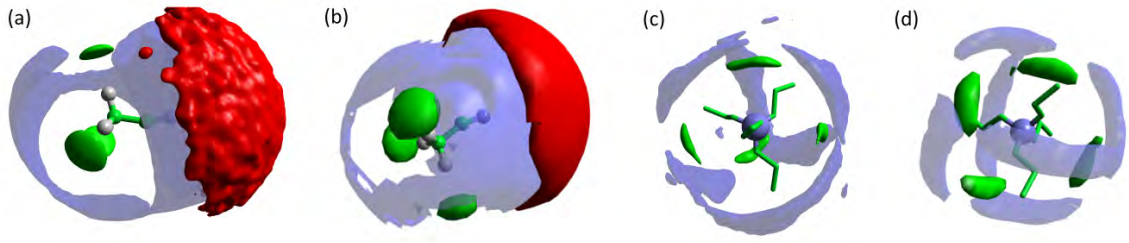

Figure 3.15.1: Spatial density distributions around (a) acn in bulk solution (b) acn in a 10 nm slit pore (c) TPA in bulk solution and (d) TPA in a 10 nm slit pore. The functions for the acn (blue), TPA (red) and Br (green) encompass surfaces representing 2.5, 2.0 and 15 times the bulk density of molecules in solution.

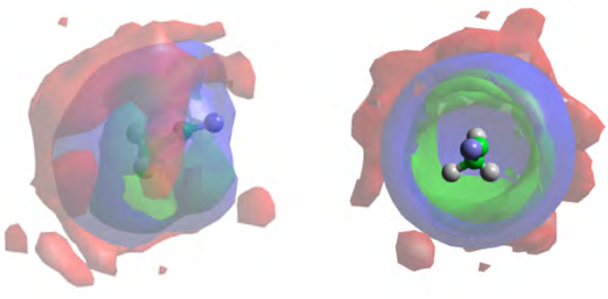

Figure 3.15.2: Spatial density distributions around acn confined in the graphene fragment pore network. The functions for the acn (blue), TPA (red) and Br (green) encompass surfaces representing 2.5, 2.0 and 15 times the bulk density of molecules in solution

3.16 Work performed on Scarf 2015-2016

Robbie Scott, Plasma Physics Group, Central Laser Facility.

I have performed a wide range of simulation work on Scarf over the last year for users of the CLF from various UK universities.

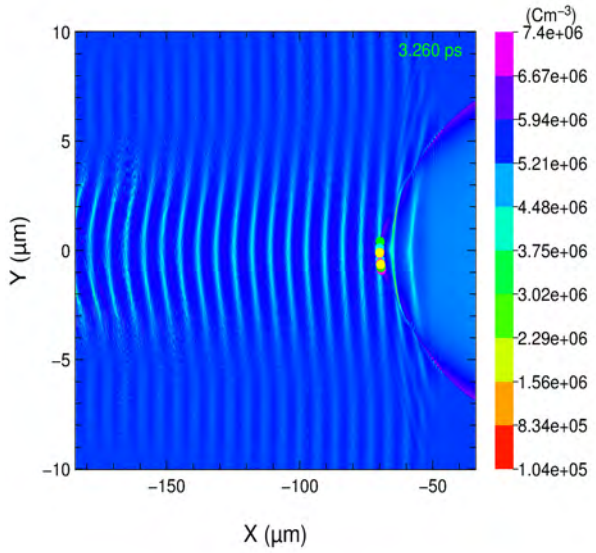

Figure 3.16.1: Particle-in-cell modelling of electron acceleration via the laser-wakefield technique. This plot shows contours of plasma charge density; the light blue curves depict the wakes driven by the laser-plasma interaction which can accelerate electrons to GeV energies (coloured dots).

University of Oxford researchers use the Central Laser Facility's Astra-Gemini laser to accelerate electrons to GeV energies using the 'plasma wakefield' technique, which, if perfected, will revolutionise future accelerator technology. Their experimental data showed some encouraging, but puzzling, results. Understanding this complex interaction required extensive use of the Scarf cluster to run a combination of the Particle-in-cell code EPOCH to capture the complex kinetics of the laser-plasma interaction, followed by radiation-hydrodynamics modelling of the hydrodynamic plasma expansion with the FLASH code, then finally a second particle-in cell modelling stage of the plasma wakefield generation. Using scarf it has been possible to gain a more complete understanding of the complex physics involved, enabling researchers to better design the next generation of electron accelerators.

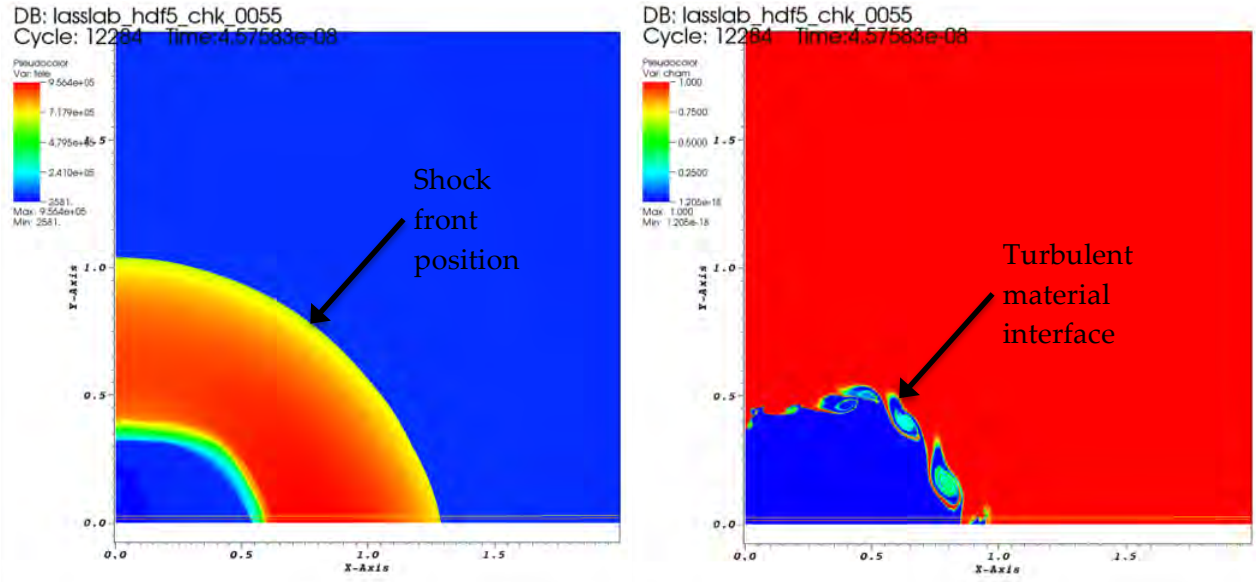

Figure 3.16.2: Left: electron temperature plots from a target after being illuminated by the Vulcan petawatt laser, showing a smooth shockwave expansion into the background plasma. Right: turbulent structures are generated via the Kelvin-Helmholtz instability at the interface

Researchers from the University of York have used the Central Laser Facility's Vulcan laser to ablate targets driving strong shock waves within solid matter compressing it to high densities and creating turbulent vortices within the ablated plasma. Running on Scarf, the FLASH 3D radiation-hydrodynamics code has been used to model the laser-plasma interactions and the conditions generated, enabling researchers to better understand their experimental data. This work has been found to have particular relevance to blast-waves, as the turbulent structures modify the blast-wave propagation velocities and shape.

Papers

Two papers are currently being drafted based on this work.

3.17 Density Functional Theory for Muon Spin Rotation and Relaxation spectroscopy

Pietro Bonfà, Ifeanyi John Onuorah, Roberto De Renzi

Department of Physics and Earth Sciences, University of Parma, Parma (Italy)

Muon spin rotation and relaxation spectroscopy (μSR) is an effective experimental technique to investigate magnetic materials. The method relies on the acquisition of the precessions of the spin of positive muons implanted in the material under study. In general, the interstitial position occupied by the muon is not known and this can prevent the estimation of certain quantitative information about the magnetic order of the sample.

To address this problem and to improve the data analysis of μSR, we use Density Functional Theory (DFT) calculations. The interaction between the muon and the electrons is evaluated using the QuantumESPRESSO package [1] which performs *ab initio* electronic structure simulations using the pseudopotential and plane waves basis approach. The method described in Refs. [2-4] allows to identify the interstitial position occupied by the muon in crystalline materials.

Using the SCARF cluster we already predicted the muon site in numerous materials [2,5-7]. This eventually permitted the characterization of the long range magnetic order of several compounds [5-7]. To quote one example, we report here on the case of MnP, the first Mn based superconductor discovered in late 2014 [8]. This material is characterized by a helical magnetic state at $T < 50$ K and ambient pressure. Under 2.5 GPa hydrostatic pressure, the magnetic order changes and two different descriptions of the high pressure magnetic state recently appeared in literature [9].

With the computational approach discussed above we identified the interstitial position occupied by the muon which allowed to estimate the hyperfine coupling terms for the muon.

This eventually permitted to compare the expected magnetic field at the muon site for the low temperature magnetic orders proposed in literature. The μSR data finally allowed to identify the antiferromagnetic long range order which is stabilized by hydrostatic pressure before the appearance of superconductivity [7].

In addition, we are also conducting a comprehensive analysis on the accuracy of *ab initio* predicted contact hyperfine fields at the muon site. While first principles approaches are found to be very accurate for the estimation of the contact hyperfine field at the nuclear sites, the contact field at the muon site is usually between one and two orders of magnitude smaller than that on the nuclei. This represent a challenge for the current accuracy of DFT based methods. Preliminary results seem to show that, with a well converged and accurately described electronic ground state, it is possible to evaluate contact hyperfine fields with an acceptable uncertainty also for μSR spectroscopy.

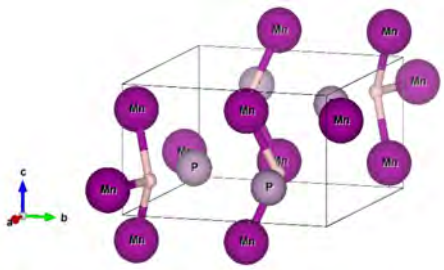

Figure 3.17.1: Interstitial position occupied by the muon (pink ball) in orthorhombic MnP.

References

[1] http://www.quantum-espresso.org

[2] P. Bonfà, F. Sartori, and R. De Renzi, *J. Phys. Chem. C* **119**, 4278 (2015)

[3] J. S. Möller, D. Ceresoli, T. Lancaster, N. Marzari, and S. J. Blundell, *Phys. Rev. B* **87**, 121108R (2013)

[4] P. Bonfà and R. De Renzi, *J. Phys. Soc. Jpn.* **85**, 091014 (2016)

[5] A. Amato, P. Dalmas de Réotier, D. Andreica, A. Yaouanc, A. Suter, G. Lapertot, I. M. Pop, E. Morenzoni, P. Bonfà, F. Bernardini, and R. De Renzi, *Phys. Rev. B* **89**, 184425 (2014)

[6] N. Martin, M. Deutsch, F. Bert, D. Andreica, A. Amato, P. Bonfà, R. De Renzi et al., *Phys. Rev. B* **93**, 174405 (2016)

[7] R. Khasanov, A. Amato, P. Bonfà, Z. Guguchia, H. Luetkens, E. Morenzoni, R. De Renzi, and N. D. Zhigadlo *Phys. Rev. B* **93**, 180509(R)

[8] J.-G. Cheng, K. Matsubayashi, W. Wu, J. P. Sun, F. K. Lin, J. L. Luo, and Y. Uwatoko, *Phys. Rev. Lett.* **114**, 117001 (2015)

[9] M. Matsuda, F. Ye, S. E. Dissanayake, J.-G. Cheng, S. Chi, J. Ma, H. D. Zhou, J.-Q. Yan, S. Kasamatsu, O. Sugino, T. Kato, K. Matsubayashi, T. Okada, and Y. Uwatoko *Phys. Rev. B* 93, 100405(R) (2016), Yishu Wang, Yejun Feng, J.-G. Cheng, W. Wu, J. L. Luo, T. F. Rosenbaum, *Nature Communications* **7**, 13037 (2016)

3.18 Hydrogen Dynamics in Condensed Matter: Linking Neutron Data to First-principles Predictions

Felix Fernandez-Alonso (ISIS), Kacper Druzbicki (JINR Dubna, AMU Poznan) and Matthew Krzystyniak (ISIS, Nottingham Trent University)

In the period 01/08/15 to 06/11/16, we continued using the SCARF cluster in research projects aimed at linking periodic DFT calculations using CASTEP to the interpretation of Compton (NCS), inelastic (INS) neutron-scattering experiments as well as neutron diffraction (ND) carried out at the ISIS Pulsed Neutron and Muon Source, Rutherford Appleton Laboratory [1- 6]. Emphasis has been placed on hydrogen-containing materials of fundamental and technological interest. Work published to date includes comparison of model calculations with experimental NCS and hydrogen dynamics in the prototypical proton conductor caesium hydrogen sulphide [1]. Review article work giving a broader overview of *in silico* methodology in the context of NCS is ongoing [2, 3]. Results of neutron and in silico work have been presented at *European Charge Density Meeting - ECDM 7, Warsaw, July, 2016* [4], *The 5th International Symposium on Energy Challenges and Mechanics - working on small scales*, Inverness, June 2016, [5], and *CECAM Workshop 'Path Integral Quantum Mechanics: Theory, Simulation and Application', Lausanne, June 2016* [6]. Brief summaries of the work accomplished to date are enclosed below.

Hydrogen Dynamics in a Solid Proton Conductor $CsHSO_4$

SCARF computational resources have been used to calculate momentum distributions in the solid proton conductor caesium hydrogen sulphide $CsHSO_4$ [1]. The motivation for this work has been threefold: (i) to investigate how much the investigation of the proton momentum distribution below the superprotonic phase transition, in the crystallographic phase III, can give insight into possible mechanism responsible for the onset of the proton conduction, (ii) to check the hypothesis that proton motions in $CsHSO_4$ are purely classical down to cryogenic temperatures, a task that can be accomplished by comparing measured and calculated proton momentum distributions and establishing how much of the measured widths of momentum distributions can be explained by classical Maxwell-Boltzmann distribution (iiii) benchmark first-principles computational models.

PW-DFT electronic structure and phonon calculations using the CASTEP code within the GGA approximation have been performed for $CsHSO_4$ (Figs. 3.18.1 and 3.18.2) and compared with experimental NCS data. Linear-response phonon calculations were employed to obtain second moments of the nuclear momentum distribution. Fair agreement with experimental values for the isotropic widths of the proton momentum distribution was achieved. Building upon this experience, we performed ab initio calculations in CASTEP within the generalised-gradient approximation, using both 'standard' and 'hard' formulations of the Perdew-Burke-Ernzerhof functional supplemented by Tkatchenko-Scheffler dispersion corrections. Both approaches provided an excellent description of the known structure, underlying vibrational density of states, and nuclear momentum distributions measured at 10 and 300 K. From this analysis, we found that only the heavier caesium atoms reach the classical limit at room temperature. Contrary to expectation, sulfur exhibited a more pronounced quantum character relative to classical predictions than the lighter oxygen atom. We interpreted this hitherto unexplored nuclear quantum effect as arising from the tighter binding environment of this species.

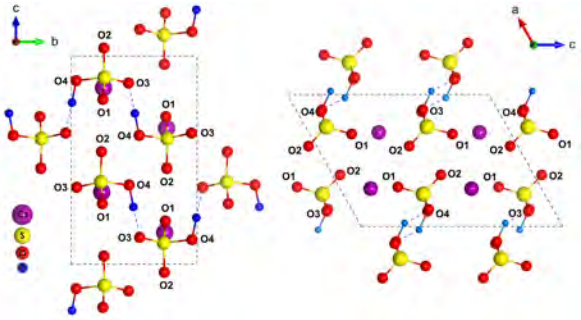

Figure 3.18.1: Structure of CsHSO4 phase III optimised with CASTEP.

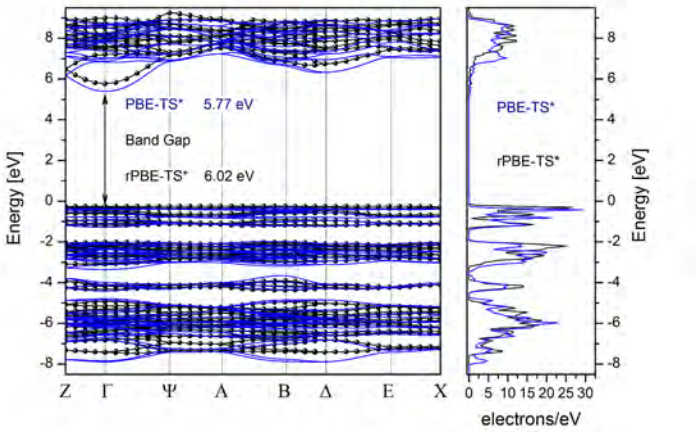

Figure 3.18.2: Electronic band-structure (left) and density-of-states (right) for CsHSO4 phase III calculated with CASTEP.

Publications & Presentations

[1] M. Krzystyniak, K. Druzbicki, and F. Fernandez-Alonso, 'Nuclear Dynamics in the Metastable Phase of the Solid Acid Caesium Hydrogen Sulfate', Physical Chemistry Chemical Physics, vol 17, 31287-31296, 2015.

[2] C. Andreani, R. Senesi, M. Krzystyniak, G. Romanelli and F. Fernandez-Alonso, 'Atomic Quantum Dynamics in Materials Science' in Experimental Methods in the Physical Sciences vol 49, F. Fernandez-Alonso and D. Price Eds, Academic Press, 2016, submitted

[3] C. Andreani, R. Senesi, M. Krzystyniak and F. Fernandez-Alonso, 'Electron-volt Neutron Spectroscopy: Beyond Fundamental Systems', Advances in Physics, 2016, submitted

[4] M. Krzystyniak and F. Fernandez-Alonso, 'Mass-selective spectroscopy of nuclear momentum distributions: ionic compounds and beyond', talk presented at the, European Charge Density Meeting – ECDM 7, Warsaw, July, 2016

[5] M. Krzystyniak, 'Nuclear dynamics in the metastable phase of the solid acid caesium hydrogen sulphate', invited talk presented at the 5th International Symposium on Energy Challenges and Mechanics – working on small scales, Inverness, July, 2016

[6] M. Krzystyniak, G. Romanelli and F. Fernandez-Alonso, 'Mass-selective neutron spectroscopy', poster presented at CECAM Workshop 'Path Integral Quantum Mechanics: Theory, Simulation and Application', Lausanne, June 2016

3.19 Effect of Radiative Cooling on Fast Electron Transport

A.P.L.Robinson and H.Schmitz

Central Laser Facility, STFC Rutherford-Appleton Laboratory

As part of the ERC funded STRUCMAGFAST project we have been developing a hybrid code for studying fast electron transport. The key feature of this hybrid code is the inclusion of radiation transport.

One possible use of relativistic electron beams generated by ultra-intense laser irradiation of solids and dense plasmas is the use of these ultra-high current beams to heat compressed fusion fuel to ignition conditions (the 'Fast Ignition' concept). In order to do this it became apparent that one would have to employ very high current beams.

In solid targets such beams would rapidly heat targets to keV temperatures. At moderate atomic numbers (e.g. Z > 20, i.e. the transition metals) the radiative cooling that one would estimate due to Lyman-alpha transitions becomes sufficiently high that radiative cooling can compete with the heating of the target due to the fast electron beam. This is a very interesting regime as this implies that radiative cooling can actually affect fast electron transport. At the very least this should impose strong limits on how strongly the solid can be heated.

Our new hybrid code KLYTEMNESTRA has been used in the past few months to start to study this new regime. Already we are finding that radiative cooling can have effects on the heating and fast electron transport that are both gross and subtle in nature.

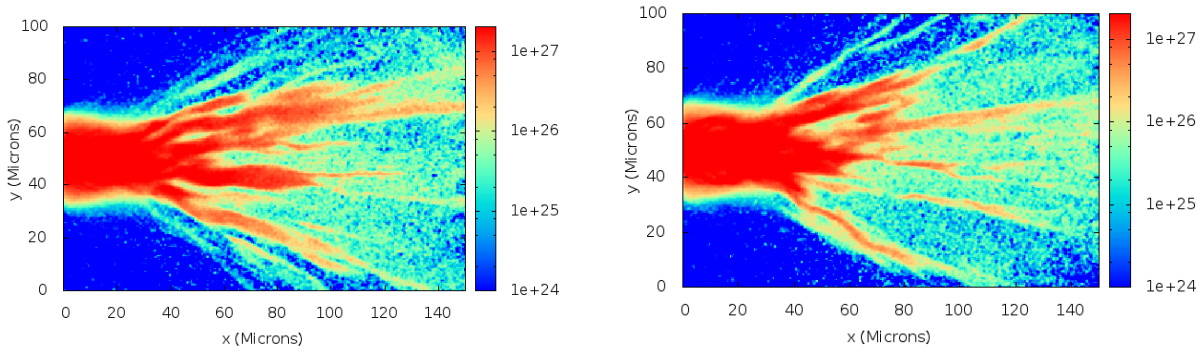

Figure 3.19.1: Fast electron density plots from KLYTEMNESTRA – (left) including radiative losses, (right) without radiative losses.

3.20 Hydration Free Energy Simulations and Beyond

Hannes Loeffler (SCD)

The accurate calculation of binding free energies is one of the grand challenge problems in computational biology. Alchemical free energy simulations provide this accuracy but are computationally very expensive and thus HPC facilities are required to tackle the problem efficiently and within a reasonable amount of time. In the past year we have been finishing a hydration free energy study and I have started to explore the effects of point mutations on ligand binding within a kinase.

We are currently in the process of writing up a manuscript on the reproducibility of the relative free energy of hydration of small organic molecules with various popular MD codes. This is a collaboration with Julien Michel (Edinburgh), David Mobley (UC Irvine, USA) and Benoit Roux (University of Chicago, USA). The MD packages AMBER, GROMACS, CHARMM and Sire have been part of the benchmark and we identified various problems that prevented successfully carrying out free energy simulations. Several bugs have been found and simulation protocols had to be worked out to properly reproduce the hydration free energy. We are now confident that we can give recommendations and suggestions for best practice to both users and developers.

Mutational changes in proteins are an important cause for development of diseases. E.g. changes to the protein sequence in the EGFR kinase are implicated in various forms of cancers and other disorders. I am currently in the process of studying mutation effects with relative alchemical free energy simulations. Previous computations with the MM-PBSA method will be used to compare the results and to judge the usefulness of the cheaper method.

FESetup is an automatic set-up tool for relative alchemical free energy simulations and the work carried out on SCARF is used to drive further development. *FESetup* has been presented in the CCPBioSim training week in Bristol, June 6th to 10th, 2016. The software has also been mentioned in the "Simulations for the Experimentalist and the Industrialist" conference, Nov 15th/16th at Diamond, RAL. Background on the code has been published in DOI:10.1021/acs.jcim.5b00368.

SCARF has proved to be an excellent resource in performing free energy simulations especially for small-scale systems. This platform enables thousands of jobs to be run very efficiently. High throughput is a particular plus of the machine. Other UK based HPC facilities demand high scalability so that small problem sizes may even be barred from running.

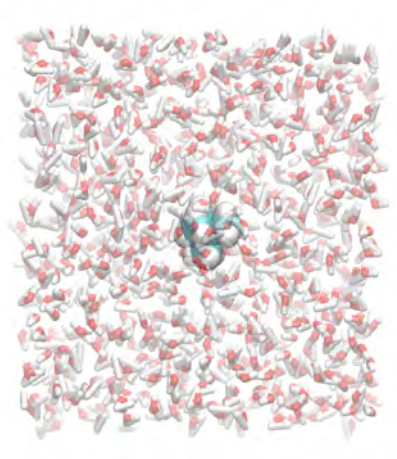

Figure 3.20.1: A small organic molecule in solution will be transformed into another one by means of thermodynamic integration.

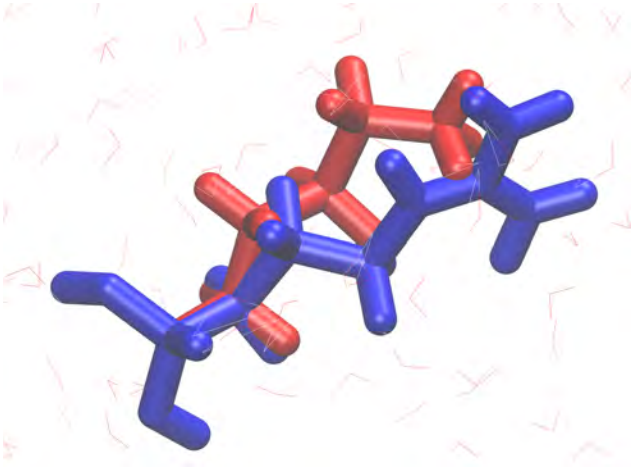

Figure 3.20.2: Mutation of Lys to Arg in a protein model system.

3.21 Looking inside catalysts through neutrons

Pedro D. Vaz (ISIS and Univ. Lisbon, PT), Carla D. Nunes (Univ. Lisbon, PT), Sam Callear (ISIS)

In nearly 80% of all compounds produced in chemical and pharmaceutical industries at least one catalytic step is essential during their synthesis. Catalysts speed up chemical reactions but can be recovered unchanged at the end of the reaction. They can also direct the reaction towards a specific product and allow reactions to be carried out at lower temperatures and pressures with higher selectivity towards the desired product. This is a principle that is pursued with increasing emphasis and dedication leading to far more specific and cleaner processes. This is part of an ongoing research in the development of more selective and efficient (overall greener) oxidation catalysts.

When styrene is used as the substrate for conducting oxidation reactions, curious phenomena arise. Under similar reaction conditions (catalyst, oxidant, solvent and temperature), the styrene oxidation reaction when carried out under exactly the same conditions yields selectively different products (styrene oxide or benzaldehyde) depending on the solvent being used (Figure 3.21.1). For instance, the styrene oxidation reaction at 353 K yields styrene epoxide or benzaldehyde, depending on whether the solvent is, respectively, acetonitrile or toluene. During the catalytic process both acetonitrile and toluene remain unreacted. A recent SANDALS experiment (RB1600022) has demonstrated that there are differences correlated with the intermolecular interactions between styrene and the solvents (acetonitrile and toluene). In particular, when acetonitrile is used, experimental data revealed the existence of H-bonds when acetonitrile is present, whereas these are absent when toluene is used instead. These data resulting from the SANDALS experiment performed on the structure of the above styrene/solvent systems using isotopic substitution and modelled with EPSR, are shown in Figure 3.21.1.

Work on SCARF by means of the Gaussian09 code is contributing to establish the missing link between neutron data and the proposed mechanism of the reaction.(Figure 3.21.1 c)

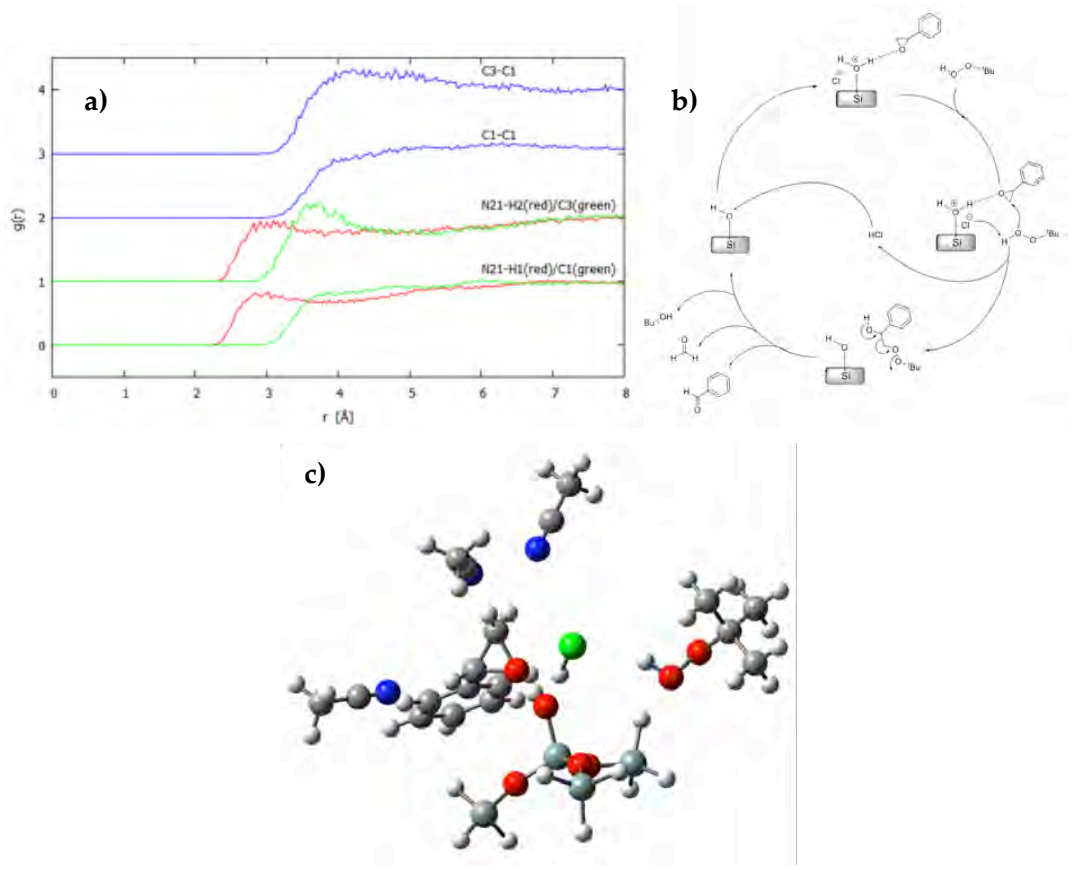

Figure 3.21.1: Preliminary partial radial distribution functions from EPSR simulation of SANDALS data from RB1600022 on the styrene: 5racetonitrile (a) data replicating the ratios used in a catalytic experiment. In (a) the N21-H2 shows clearly the existence of H-bonding between the acetonitrile *N*-atom and H-atoms in the vinyl group of styrene. (b) Proposed mechanism for oxidation of styrene oxide to benzaldehyde. (c) Hypotetic structure of styrene oxide with peroxide, HCl and acetonitrile solvent molecules [right, similar to the structure drawn on the right side of the catalytic cycle in the scheme shown in (b)] as obtained from DFT calculations. The DFT geometry is the result of the interpretation of SANDALS experimental neutron scattering data.

3.22 Deep Eutectic Solvents assessed by neutron scattering

Mariela Nolasco (Univ. Aveiro, PT), Paulo Ribeiro Claro (Univ. Aveiro), Pedro D. Vaz (ISIS and Univ. Lisbon, PT), Svemir Rudic (ISIS)

Deep Eutectic Solvents (DESs) are formed by the association of a hydrogen bond-capable salt (frequently ammonium halides) with a neutral hydrogen bond donor species (HBD). In the eutectic composition, the mixture has a melting point much lower than either of the individual components. A significant deep eutectic phenomenon was observed for a mixture of choline chloride and urea in a 1:2 mole ratio. The resulting mixture has a melting point of 12 °C (far less than the melting point of choline, 302 °C and urea, 133 °C), which makes it liquid at room temperature.

These systems are emerging as potentially tuneable non-toxic and biodegradable solvents for a wide range of applications, including transformations of cellulose and starch, and purification and manufacturing of biodiesel – themes of particular interest for CICECO - Aveiro Institute of Materials. Since DESs constituents include ions and a molecular hydrogen bond donor species, the nature of the hydrogen bond network among these constituents is expected to play a significant role in the structure and dynamics of a DES and on its properties as solvent. In fact, the key physical driving force for the formation of DESs is generally attributed to charge delocalization between the anion and HBD upon mixing as a result of the formation of hydrogen bonds. In this way, the study of hydrogen bond networks in DESs – which will allow the design of solvents according to the purposes - is currently a subject of high scientific interest.

The research Lab CICECO - Aveiro Institute of Materials has a good track record on the study of phase transition problems with industrial relevance, including Ionic Liquids and, more recently, DESs. The collaboration between the engineering group and the vibrational spectroscopy group – namely in problems related with hydrogen bonding is highly relevant in this theme (DES).

Using the CASTEP code on SCARF is contributing to establish the structure of these promising solvents and making a relevant contribution to the field. So far, the team came up with a reasonable proposal for the structure of DES between choline chloride and urea (Figure 3.22.1). The simulated data has provided useful insight that is now being worked out for an upcoming publication.

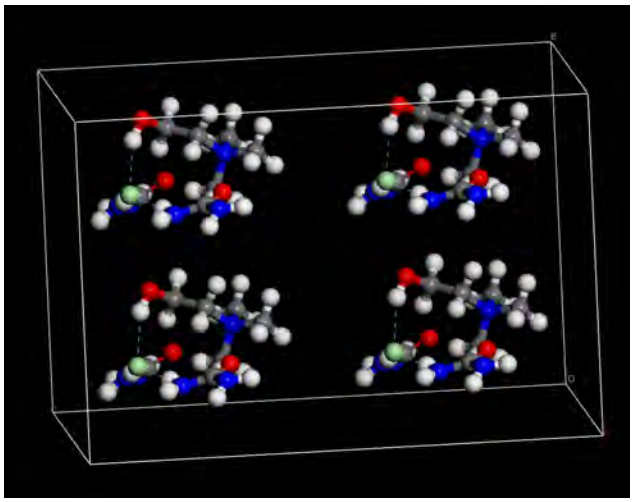

Figure 3.22.1: Optimized geometry for the choline chloride:urea DES as obtained by CASTEP simulations.

3.23 Association of aescin with β- and γ-cyclodextrins studied by ab initio and spectroscopic methods

Ana I. Ramos (Univ. Aveiro, PT), Pedro D. Vaz (ISIS and Univ. Lisbon, PT), Susana S. Braga (Univ. Aveiro, PT) and Artur M. Silva (Univ. Aveiro, PT)

Aescin, a natural mixture of saponins occurring in *Aesculus hippocastanum*, exhibits important phlebotonic properties, being thus used in the treatment of chronic venous insufficiency in legs. The association of aescin with cyclodextrins (CDs) is used as technical solution for its incorporation into stockings, but details of the physico-chemistry of these host-guest systems are lacking. In this work we investigated the inclusion of aescin into the cavities of two native cyclodextrins, β-CD and γ-CD.

Work on SCARF using DFT calculations (Density Functional Theory; Gaussian09 code) on the interaction of aescin 1b with CDs has shown that inclusion can indeed occur and that the wider cavity of γ-CD is more adequate to accommodate this large guest. DFT calculations were also applied to determine the chemical shifts of the protons H3 and H5 of the CDs in the optimised structures of the inclusion complexes. The calculated values are very similar to the experimental data, validating the approach made in this study by solution NMR. The combination of experimental data from aqueous-state NMR measurements and theoretical calculations has demonstrated that γ-CD is the most suitable host for aescin, although the inclusion also occurs with β-CD. The DFT calculations afforded two possible geometries for γ-CD·aescin.

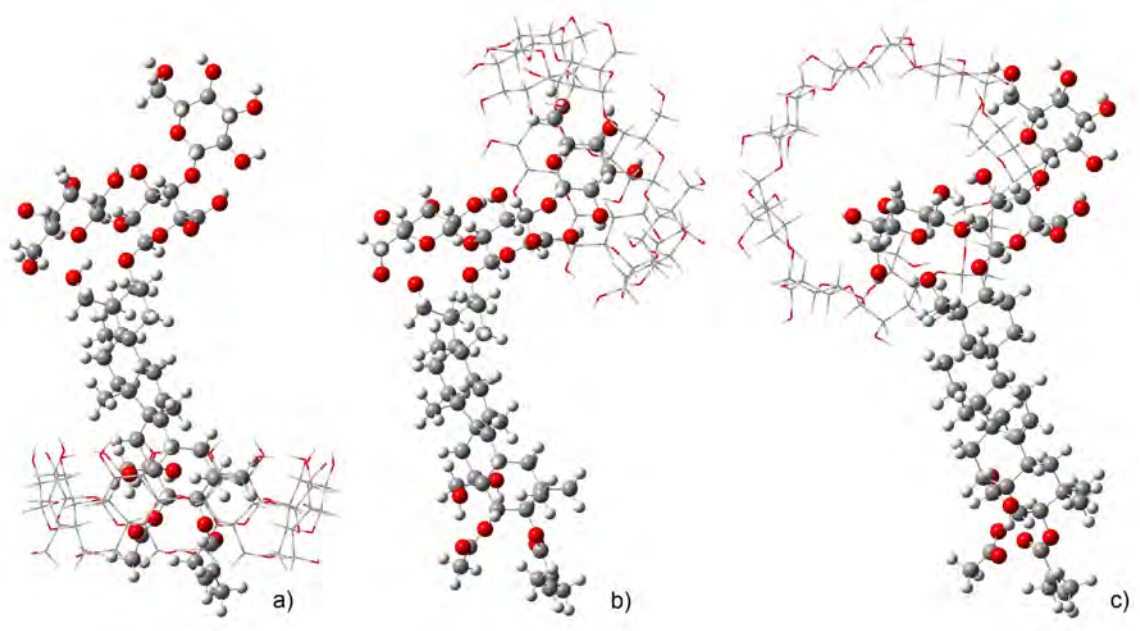

Figure 3.23.1: Optimised geometries for three different hypothetical structures of γ-CD·aescin. The structures have the same orientation to facilitate viewing.

3.24 Global Monitoring of cloud properties from Space

Caroline Poulsen, Matt Christiansen, Gareth Thomas - Remote Sensing group, RAL Space

Clouds and aerosols contribute the largest uncertainty to estimates and interpretations of the Earth's changing energy budget[1]. Clouds have long been recognised as one of the key moderators of the Earth's atmosphere: low clouds such as stratus effectively reflect incoming solar radiation, giving an overall cooling effect, while high clouds may partially transmit solar radiation, but effectively trap the outgoing thermal radiation, resulting in an overall warming effect. Aerosols of anthropogenic origin are responsible for a radiative forcing of climate change through their interaction with radiation, and also as a result of their interaction with clouds. Quantification of this forcing is fraught with uncertainties. We have been using Scarf to produce climatology of cloud properties from the ATSR (Along Track Scanning Radiometer) series of satellite instruments using the ORAC (Optimal Retrieval of Cloud and Aerosol) algorithm [3][4]. The algorithm is being applied in the ESA (European Space Agency) Aerosol and Cloud CCI (Climate Change Initiative).

Figure 3.24.1 shows the rends in cloud height and coverage for the years 2002-2012 using the AATSR instrument

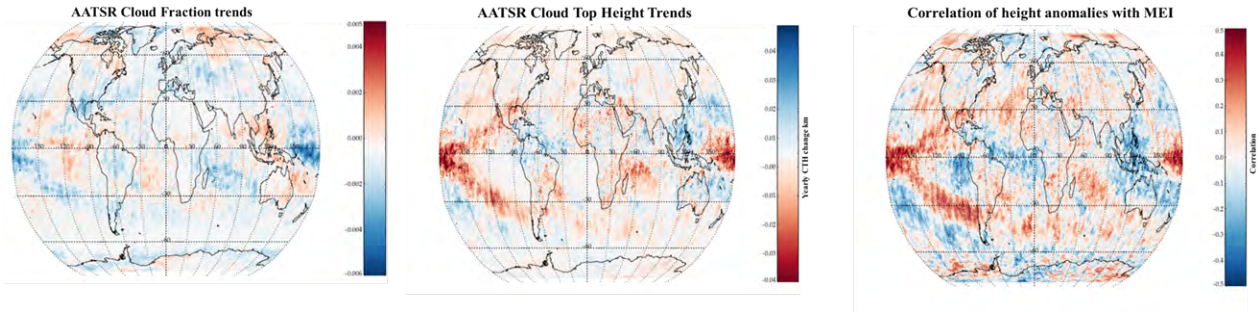

Figure 3.24.1: Trend in cloud fraction, left, cloud height, centre and the correlation with the MEI right.

The trends were calculated using the Theil-Sen slope estimator and the Mann-Kendall (MK) significance test were selected for trend analysis as these are non-parametric and robust for not normally distributed data with missing values. Both test each point in the series against every following point, with the MK test comparing the total increases-decreases with a random distribution, and the Sen slope taking the mean slope as described by the following:

$$sopel=median\{(y\_i-y\_j)/(x\_i-x\_j\ ),\ i>j\}$$

Both the Sen slope estimate and the Mann-Kendall test statistic used can be biased by serial correlation in the data, so this was removed using the "pre-whitening" process by Yue et al[2].

Cloud top height is shown to decrease globally over this period, see Fig. 3.24.1, centre, and the cloud amount, left, to decreases over the same period. The figure to the right shows the cloud top height anomalies for each month correlated with the MEI (Multi Variate ENSO (El Nino Southern Oscillation) Index). The changes in cloud properties are shown to be strongly linked with ENSO events. When the influence of the ENSO events is removed then the trends in cloud properties are not significant.

References

[1] IPCC, Climate Change 2013: The Physical Science Basis. Contribution of Working Group I to the Fifth Assessment Report of the Intergovernmental Panel on Climate Change. Cambridge University Press, Cambridge, United Kingdom and New York, NY, USA.

[2] Yue, S., et al., 2002:The influence of autocorrelation on the ability to detect trend in hydrological series, Hydrol. Process., 16, 1807–1829

[3] Poulsen, C. A., Siddans, R., Thomas, G. E., Sayer, A. M., Grainger, R. G., Campmany, E., Dean, S. M., Arnold, C. and Watts, P. D.: Cloud retrievals from satellite data using optimal estimation: evaluation and application to ATSR, Atmos. Meas. Tech., 5(8), 1889-1910, 2012.

[4] Thomas, G. E., Carboni, E., Sayer, A. M., Poulsen, C. A., Siddans, R. and Grainger, R. G.: Oxford-RAL Aerosol and Cloud (ORAC): aerosol retrievals from satellite radiometers. In Satellite aerosol remote sensing over land, Kokhanovsky, A. A. & de Leeuw, G. (eds.), Springer-Praxis, 193-225, 2009.

3.25 Optimisation of Electron Storage Ring Design using a Multi-Objective Genetic Algorithm

I.P.S Martin, M. Apollonio, R. Bartolini, M. Furseman

Diamond Light Source, Oxfordshire, UK

The next generation of ultra-low-emittance electron storage rings will deliver x-ray beams to users with unprecedented levels of brightness and transverse coherence. These rings required high-gradient quadrupole and sextupole magnets to store the beam, resulting in a substantial reduction in stable oscillation amplitudes for the electrons compared to earlier generations. This in turn can potentially lead to a drop in lifetime and injection efficiency.

In order to mitigate this reduction and to maximise machine performance, a careful tuning of all magnet strengths is required. Whilst analytical techniques exist to do this [1], approximations and simplifications are necessarily introduced in this analysis, limiting their validity. As such, studies often resort to large-scale particle tracking simulations either to optimise the design or to validate final solutions. These studies involve tracking large numbers of particles over many turns to determine the stability of the electrons, thereby giving an estimate of lifetime and injection efficiency in the presence of realistic magnet field profiles and alignment.

In recent years, the use of evolutionary algorithms to aid storage ring design and performance has become widespread (see for example [2-4]). One such algorithm is the Non-dominated Sorting Genetic Algorithm (NSGA-II, [5]). In this, an initial population of potential solutions are assessed for fitness against one or more criteria, with those solutions that best meet the criteria selected for further breeding and mutation. At the end of each generation, a so-called Pareto-optimal front is produced, illustrating the members of each generation that are not dominated by any other member simultaneously in more than one objective. Due to the large number of population members and length of time required to calculate the lifetime and injection efficiency for each solution, large scale, high-performance computing clusters such as SCARF are a pre-requisite for applying such algorithms to storage ring design. With these, the calculation of lifetime and injection efficiency can be distributed and parallelised for each solution, reducing the time to simulate to practical values.

The NSGA-II algorithm has been applied to the optimisation of the Diamond Double-Double Bend Achromat (DDBA) storage ring lattice modification [6]. Extensive use of the SCARF cluster was made, optimising the machine performance for several operating modes [7]. Figure 3.25.11 presents an example Pareto front from one such optimisation run, and the resulting off-momentum dynamic aperture for the best solution is shown in Fig. 3.25.2. Thanks in part to this work, the DDBA lattice modification was successfully installed and commissioned during Autumn 2016.

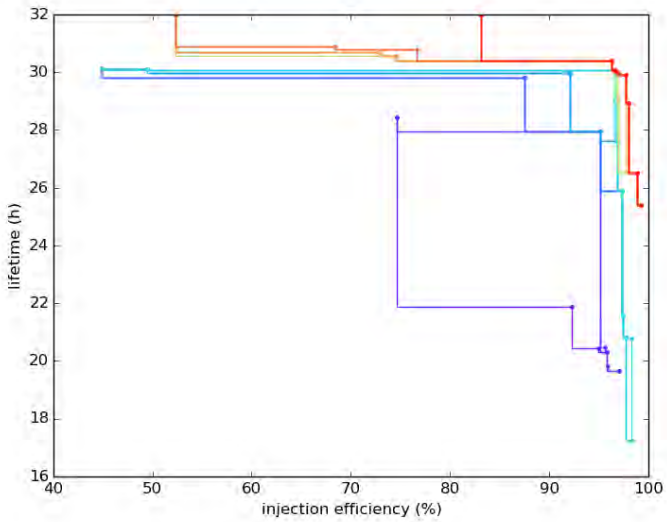

Figure 3.25.1: Pareto fronts for an NSGA-II optimisation of the Diamond storage ring. Different colours represent different orders of the front, with the leading front shown in red.

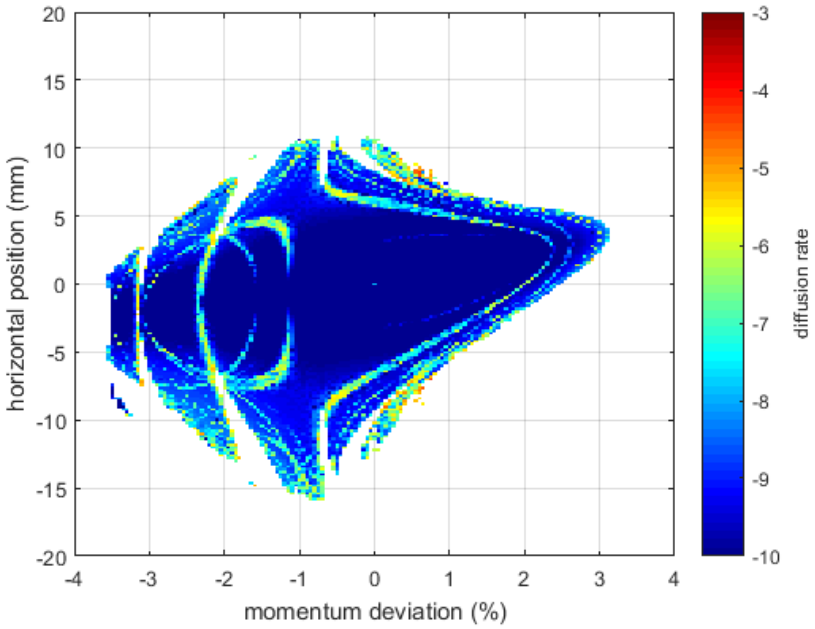

Figure 3.25.2: Region of stable particle motion for the Diamond DDBA modified storage ring.

References

[1] R. Bartolini, Proc. Int.l Particle Accelerator Conference 2016, Busan, Korea, MOZA02, (2016)

[2] M. Borland, V. Sajaev, L. Emery, A. Xiao, Technical Note ANL/APS/LS-319, (2010)

[3] X. Huang, J. Safranek, Nucl. Inst. And Meth. In Phys. Res. A 757, 1, pp. 48-53, (2014)

[4] M.P. Ehrlichman, Phys. Rev. Accel. Beams 19, 044001, (2016)

[5] K. Deb, A. Pratap, S. Agarwal, T. Meyarivan, IEEE Trans. On Evolutionary Computation 6, 2, pp 182-197, (2002)

[6] R.P. Walker et al., Proc. Int. Particle Accel. Conf. 2014, Dresden, Germany, MOPRO103, (2016)

[7] I.P.S. Martin, R. Bartolini, Proc. Int. Particle Accel. Conf. 2015, Richmond, USA, MOPMA002, (2015)

3.26 Report on Work Performed on SCARF

Marta Falkowska and Tristan Youngs, ISIS

MCM-41 type mesoporous materials, *i.e*. amorphous silica with unidimensional cylindrical pores in a hexagonal array are widely used as a catalyst's support. This is mainly due to a sharp pore distribution, a large surface area, a large pore volume and excellent thermal and mechanical stability. In the typical heterogeneous system utilising such a catalyst's support, the reaction occurs on the active sites distributed inside a pore, and liquid reagents are confined within pores. The thermodynamical and structural properties of confined liquids, such as phase transition pressures, temperatures, density and diffusion, are different from these in the corresponding bulk phase. This is due to the reduced dimensionality and large interface effect that impact the structure of a liquid. Heterogeneous catalysts are almost four times more frequently used than homogeneous systems,[1] but the design of industrial catalytic processes involving these systems is largely empirical. Understanding the effects of confinement on the reagents structure could lead to significant improvements of these processes.

Herein, we used total neutron scattering to obtain an insight into a structure of three commonly used in production processes solvents – cyclohexane, cyclohexene and benzene confined in MCM-41, which was then compared with the bulk phase. The neutron experiments were undertaken on the Near and InterMediate Range Order Diffractometer (NIMROD) on the ISIS Second Target Station at the Rutherford Appleton Laboratory. Total neutron scattering measurements were taken for the evacuated catalyst and the catalyst filled with cyclohexane, cyclohexene and benzene. Raw neutron datasets were processed using GUDRUN[2] and analysis of the data proceeded *via* refinement of atomistic models of the target systems using Empirical Potential Structure Refinement (EPSR).[2]

Data analysis required constructing five different models[3] of increasing complexity in disorder: MCM-41 (only Si and O atoms), MCM-41 with silanol groups (Si and O atoms, as well as H_2O molecules mimicking the presence of hydroxyl groups on the surface and in the bulk silica[4]) and MCM-41 with silanol groups filled with a compound, *i.e*. cyclohexane-d_{12}, cylcohexene-d_{10} and benzene-d_6. Finding the correct parameters describing the disordered system under studies, such as pore radius, unit cell size, concentration of water molecules, number of molecules of the given compound inserted into a pore, requires setting up the whole range of EPSR simulations. To achieve this a lot of computing power is necessary and the use of the STFC cluster SCARF was crucial.

In Figure 3.26.1 EPSR-simulated total structure factors for empty MCM-41 (unit cell size: 45.35 Å, pore radius: 15 Å, pore length: 50 Å), MCM-41 with silanol groups and filled with benzene-d_6 show good agreement with experimental data so the latter model can be used for the determination of structural properties of confined benzene-d_6. Discrepancies in the Bragg peak region in the simulation with benzene-d_6 are most likely due to the fact that some pores in the real system are under filled and some even not accessible for aromatic molecules at all, so the intensities of these peaks are not reproduced properly by EPSR. A few simulations with different number of benzene-d_6 molecules have been performed and the calculated structural properties show the same trends.

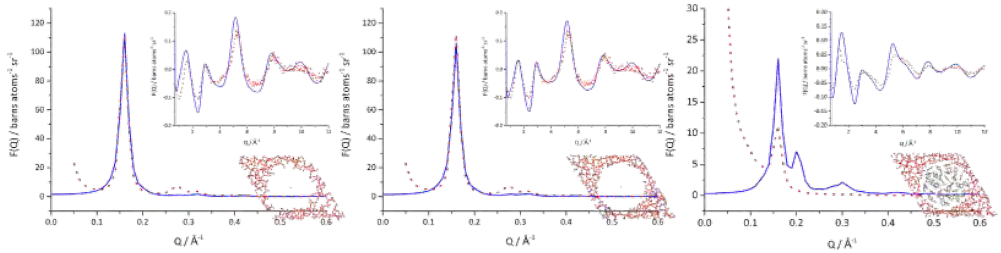

Figure 3.26.1: EPSR-Simulated total structure factors (solid lines) presented here show satisfactory fits with experimental data (symbols) for empty MCM-41 consisting of 1031 Si atoms, 2062 O atoms), MCM-41 decorated with silanol groups in ratio Si:H 0.3 and MCM-41 filled with 190 benzene-d_6 molecules.

References

[1] K. P. de Jong, in Synthesis of Solid Catalysts, Wiley-VCH Verlag GmbH & Co. KGaA, Weinheim, **2009**, 1, 1-11.

[2] Soper, A. K.; RAL Technical Reports RAL-TR-2011-013, **2011**.; Soper, A. K.; RAL Technical Reports RAL-TR-2011-012, **2011**.; Youngs, T. G. A.; dlputils, version 1.4.1; http://www.projectaten.net/dlputils

[3] Soper, A. K.; *Chem. Phys. Lett*., **2013**, 590, 1.

[4] Ide, M. et *al. Phys. Chem. Chem. Phys*. **2013**, 15, 642.5.

4 APPENDIX: SCARF HARDWARE DETAILS

Host group	CPU type and frequency	Nodes	Cores /node	Total cores	Interconnect	Total memory
SCARF16/ MagnaCarta/ IBIS	Intel E5-2650v3 @ 2.30GHz	56	20	1120	FDR Infiniband	7168 GB
SCARF15	Intel E5-2650v3 @ 2.30GHz	68	20	1360	FDR Infiniband	8704 GB
SCARF14	Intel E5-2650v2 @ 2.60GHz	56	16	896	QDR Infiniband	7168 GB
SCARF13	Intel E5-2660 @ 2.20GHz	84	16	1344	QDR Infiniband	5376 GB
SCARF12	Intel X5675 @ 3.06GHz	20	12	240	QDR Infiniband	960 GB
SCARF11	Intel X5660 @ 2.8GHz	32	12	384	QDR Infiniband	768 GB
Lexicon-2/ SCARF10	Intel E5530 @ 2.40GHz	104	8	832	DDR Infiniband	2496 GB
Grand Totals		**420**		**6176**		**32460 GB**

5 APPENDIX: INDEX OF FIGURES

6 APPENDIX: PUBLICATIONS AND PRESENTATIONS

6.1 Publications

	Title	Authors	Journal
1	"The effect of grading the atomic number at resistive guide element interface on magnetic collimation"	R. A. B. Alraddadi, A. P. L. Robinson, N. C. Woolsey and J. Pasley	Physics of Plasmas, 23(7)(2016): 072706.
2	"Applications of neutron scattering to heterogeneous catalysis"	S.F. Parker and D. Lennon	*Journal of Physics Conference Series*, 746 (2016) 012066. [doi: 10.1088/1742-6596/746/1/012066].
3	"Amides do not always work: observation of guest binding in an amide-functionalised porous host"	O. Benson, I. da Silva, S.P. Argent, R. Cabot Mesquida, M. Savage, H.G.W. Godfrey, Y. Yan, S.F. Parker, P. Manuel, M.J. Lennox, T. Mitra, T.L. Easun, W. Lewis, A.J. Blake, E. Besley, S. Yang and M. Schröder	*Journal of the American Chemical Society*, (2016) [doi: 10.1021/jacs.6b08059]
4	"Assignment of the vibrational spectra of the parent polysilsesquioxane (POSS): octahydridosilasequioxane, $H_8Si_8O_{12}$"	S.F. Parker	*Spectrochimica Acta A: Molecular and Biomolecular Spectroscopy* 171 (2016) 222–228. [doi: 10.1016/j.saa.2016.08.009]
5	"Neutron scattering study of the terminating protons in the basic structural units of non-graphitising and graphitising carbons"	P.W. Albers, W. Weber, K. Möbus, S.D. Wieland and S.F. Parker	*Carbon* 109 (2016) 239-245 [doi:10.1016/j.carbon.2016.08.007].
6	"The application of inelastic neutron scattering to investigate the interaction of methyl propanoate with silica"	A.R McFarlane, J.M. McNamara, H. Geller, I.P. Silverwood, R.I. Cooper, D.J. Watkin, C.D. Frost, S.F. Parker, J.M. Winfield and D.	*Physical Chemistry Chemical Physics* 18 (2016) 17210-17216 [doi: 10.1039/c6cp01276k]

		Lennon	
7	"The reaction of formic acid with Raney™ copper"	S.K. Callear, I.P. Silverwood, A. Chutia, C.R.A. Catlow and S.F. Parker	*Proceedings of the Royal Society A* 472 (2016) 20160126. [doi: /10.1098/rspa.2016.0126]
8	"The adsorbed state of a thiol on palladium nanoparticles"	S.M. Rogers, N. Dimitratos, W. Jones, M. Bowker, A.G. Kanaras, P.P. Wells, C.R.A. Catlow, and S.F. Parker	*Physical Chemistry Chemical Physics* 18 (2016) 17265-17271 [doi: 10.1039/C6CP00957C].
9	"Direct hydrodeoxygenation of raw woody biomass into liquid alkanes"	Q. Xia, Z. Chen, Y. Shao, X. Gong, H. Wang, X. Liu, S.F. Parker, X. Han, S. Yang and Y. Wang	*Nature Communications* 7 (2016) 11162. [doi: 10.1038/ncomms11162]
10	"Stabilization of 3d-transition metal hydrido complexes in $SrH_2Mg_2[Co(I)H_5]$, $BaH_2Mg_5[Co(-I)H_4]_2$ and $RbH_2Mg_5[Co(-I)H_4$ $Ni(0)H_4]$ via easily polarizable hydride ligands"	H. Fahlquist, D. Moser, D. Noréus, K. Refson, S.F. Parker,	*Inorganic Chemistry* 55 (2016) 3576-3582 [doi: 10.1021/acs.inorgchem.6b00074]
11	"Structure/activity relationships applied to the hydrogenation of α,β-unsaturated carbonyls: the hydrogenation of 3-butyne-2-one over alumina-supported palladium catalysts"	C.G.A. Morisse, A.R. McInroy, C. Anderson, I.P. Silverwood, N.G. Hamilton, C.J. Mitchell, S.F. Parker and D. Lennon	*Catalysis Today* (2016) [doi:10.1016/j.cattod.2016.02.028]
12	"Characterisation of the surface of freshly prepared precious metal catalysts",	S.F. Parker, D. Adroja, M. Jiménez-Ruiz, M. Tischer, K. Möbus, S.D. Wieland and P. Albers	*Physical Chemistry Chemical Physics* 18 (2016) 17196-17201. [doi: 10.1039/C6CP01027J]
13	"Metastable nitric acid	F. Weiss, F. Kubel, Ó. Gálvez, M.	*Angewandte Chemie*

	trihydrate in ice clouds",	Hoelzel, S.F. Parker, R. Iannarelli, M.J. Rossi, T. Peter and H. Grothe	*International Edition*, 55 (2016) 3276-3280. [doi: 10.1002/anie.201510841]
14	Explaining the mechanical mechanisms of zeolitic metal–organic frameworks: revealing auxeticity and anomalous elasticity	M.R. Ryder and J.C. Tan,	Dalton Trans., 45, 4154 (2016).
15	Isoreticular zirconium-based metal–organic frameworks: discovering mechanical trends and elastic anomalies controlling chemical structure stability	M.R. Ryder, B. Civalleri and J.C. Tan,	Phys. Chem. Chem. Phys., 18, 9079 (2016).
16	Discovering connections between terahertz vibrations and elasticity underpinning the collective dynamics of the HKUST-1 metal–organic framework	M.R. Ryder, B. Civalleri, G. Cinque and J.C. Tan,	CrystEngComm, 18, 4303 (2016).
17	Unexpected Cation Dynamics in the Low-temperature Phase of Methylammonium Lead Iodide – The Need for Improved Models	K. Drużbicki, R. Pinna, S. Rudic, M. Jura, G. Gorini, and F. Fernandez-Alonso	2016. Submitted to the Journal of Physical Chemistry Letters. DOI: 10.1021/acs.jpclett.6b01822.
18	"Neutron beam profile characterization on TOSCA"	R. Pinna, S. Parker, M. Capstick, D. McPhail, D. Pooley, G. Howells, G. Gorini, F. Fernandez-Alonso, and S. Rudic	In preparation
19	Magnetic ground state and spin fluctuations in MnGe chiral magnet as studied by muon spin rotation	N. Martin, M. Deutsch, F. Bert, D. Andreica, A. Amato, P. Bonfà, R. De Renzi et al.	Phys. Rev. B **93**, 174405 (2016)
20	High-pressure magnetic state of MnP probed by means of muon-spin rotation	R. Khasanov, A. Amato, P. Bonfà, Z. Guguchia, H. Luetkens, E. Morenzoni, R. De Renzi, and N. D. Zhigadlo	Phys. Rev. B **93**, 180509(R).
21	"Nuclear Dynamics in the Metastable Phase of the Solid Acid Caesium Hydrogen	M. Krzystyniak, K. Druzbicki, and F. Fernandez-Alonso	Physical Chemistry Chemical Physics, vol 17, 31287-31296, 2015

	Sulfate"		
22	"Atomic Quantum Dynamics in Materials Science"	C. Andreani, R. Senesi, M. Krzystyniak, G. Romanelli and F. Fernandez-Alonso	Experimental Methods in the Physical Sciences vol 49, F. Fernandez-Alonso and D. Price Eds, Academic Press, 2016, submitted
23	"Electron-volt Neutron Spectroscopy: Beyond Fundamental Systems"	C. Andreani, R. Senesi, M. Krzystyniak and F. Fernandez-Alonso	Advances in Physics, 2016, submitted
	"Association of aescin with β- and γ-cyclodextrins studied by DFT calculations and spectroscopic methods"	P. Duarte Vaz	Bielstein Journal of Nanotechnology, submitted
	"Looking inside catalysts through neutrons"	P. Duarte Vaz	Manuscript in preparation

6.2 Presentations

	Conference	Title	Presenter
1	Biochemical Society Training Day September 2016	Advanced Data Collection for High Resolution cryoEM: How to make the most of your National Facility Visit	M.Winn
2	CECAM-2016 Chemical Energy at the Nanoscale: Simulation Meets Experiment, Zaragoza, Spain	Invited lecture: "Applications of neutron scattering to catalysts and energy materials"	S. Parker
3	213th IRDG meeting, Renishaw, Wooton-under-Edge	Invited lecture: "Catalyst studies with neutrons and photons"	S. Parker
4	Scattering anelastico di neutroni: Opportunità scientifiche da strumentazione innovativa Perugia, Italy	Invited lecture: "Applicazioni degli strumenti per la spettroscopia vibrazionale"	S. Parker
5	*The 2nd CCPBioSim/CCP5 Multiscale Modelling Conference*, Manchester	**Presentation:** Density Transferability via Coarse Graining of two molecules: the case of lipids	A. Brukhno

6	5th International Conference on Metal-Organic Frameworks, California, USA	Discovering Connections between Terahertz Vibrations and Mechanical Properties Using Neutron and Synchrotron Spectroscopy	M.R. Ryder
7	Diamond Synchrotron Radiation User Meeting (SRUM), Chilton, UK – September 2016	Discovering Connections Between Terahertz Vibrations and Elasticity	M.R. Ryder
8	Advanced Research Computing: High Performance Computing Showcase "Bringing HPC Alive", Oxford, UK – April 2016	Quantum Mechanics and Terahertz Vibrations Reveal How Materials Can Breathe	M.R. Ryder
9	39th Annual Meeting of the British Zeolite Association, Bath, UK – March 2016	Explaining the Mechanical Stability of MOFs and How Terahertz Vibrations and Collective Dynamics Can Reveal The Complex Mechanisms	M.R. Ryder
10	Advances in Terahertz Spectroscopy, Cambridge, UK – March 2016	Terahertz Vibrations in Metal-Organic Frameworks: From Gate-Opening Phenomenon to Shear-Driven Structural Instability –	M.R. Ryder
11	RSC Energy Sector Early Career Chemists Symposium, London, UK – March 2016	Terahertz Vibrations of MOFs using Synchrotron and Neutron Spectroscopy in Conjunction with Ab Initio Density Functional Theory	M.R. Ryder
12	CP2K UK Users Meeting, London, UK – March 2016	Terahertz Vibrations in Metal-Organic Frameworks: From Gate-Opening Phenomenon to Shear-Driven Structural Instability	M.R. Ryder
13	Oxford Solid Mechanics Junior Event, Oxford, UK – February 2016	Explaining the Stability of Next-Generation Materials at the Molecular Level	M.R. Ryder
14	ISIS Student Meeting 2015, Abingdon, UK – October 2015	Revealing the Physical Possibilities of Framework Materials at the Molecular Level	M.R. Ryder
15	Joliot-Curie Conference 2015, Cambridge, UK – September 2015	Terahertz Vibrations in Metal-Organic Frameworks: From Gate-Opening Phenomenon to Shear-	M.R. Ryder

		Driven Structural Instability	
16	Diamond Synchrotron Radiation User Meeting (SRUM), Chilton, UK – September 2015	How Terahertz Vibrations can Reveal Pore Breathing and Structural Instability in Metal-Organic Frameworks	M.R. Ryder
17	Conference ECNS 2015, Zaragoza (Spain), 30 August – 4 September 2015	Poster presentation: *Monte Carlo modeling of TOSCA neutron spectrometer: capability benchmarking and design of the beamline upgrade*	R. Pinna, G. Gorini, S. Rudic, F. Fernandez-Alonso
18	Conference QENS and WINS 2016, Berlin (Germany), 4 – 9 September 2016	Poster presentation: *TOSCA neutron-beam characterisation along the primary spectrometer*	R. S. Pinna, S. Rudić, S. F. Parker, M. Capstick, D. McPhail, D. Pooley, G. Howells, G. Gorini, F. Fernandez-Alonso
19	18th International Seminar on Neutron Scattering in Condensed Matter, 12-14th May **2016**, Poznan, Poland.,	Invited talk: *Chemical Dynamics and Spectroscopy with Pulsed Neutrons: Recent Developments and Perspectives*	F. Fernandez-Alonso
20	SuperFOx, September 2016, Torino, Italy (http://superfox2016.polito.it) at	Poster presentation: 'Magnetic states of MnP under hydrostatic pressure'	P. Bonfà
21	Materials2016, December 2016, Catania, Italy (http://eventi.cnism.it/materials2016/)	Oral presentation (accepted): 'Magnetic states of MnP under hydrostatic pressure'	P. Bonfà
22	European Charge Density Meeting - ECDM 7, Warsaw, July, 2016	'Mass-selective spectroscopy of nuclear momentum distributions: ionic compounds and beyond'	M. Krzystyniak and F. Fernandez-Alonso.
23	5th International Symposium on Energy Challenges and Mechanics - working on small scales, Inverness, July, 2016	Invited talk: 'Nuclear dynamics in the metastable phase of the solid acid caesium hydrogen sulphate',	M. Krzystyniak

24	CECAM Workshop 'Path Integral Quantum Mechanics: Theory, Simulation and Application', Lausanne, June 2016	Poster 'Mass-selective neutron spectroscopy'	M. Krzystyniak, G. Romanelli and F. Fernandez-Alonso
25	UK Neutron and Muon Science and User Meeting	Poster Session	M. Falkowska
26	ISIS Student Meeting	Poster presentation	M. Falkowska

7 APPENDIX: SCARF QUEUE USAGE 2015-16

7.1 General SCARF Queue

Open to all SCARF Users

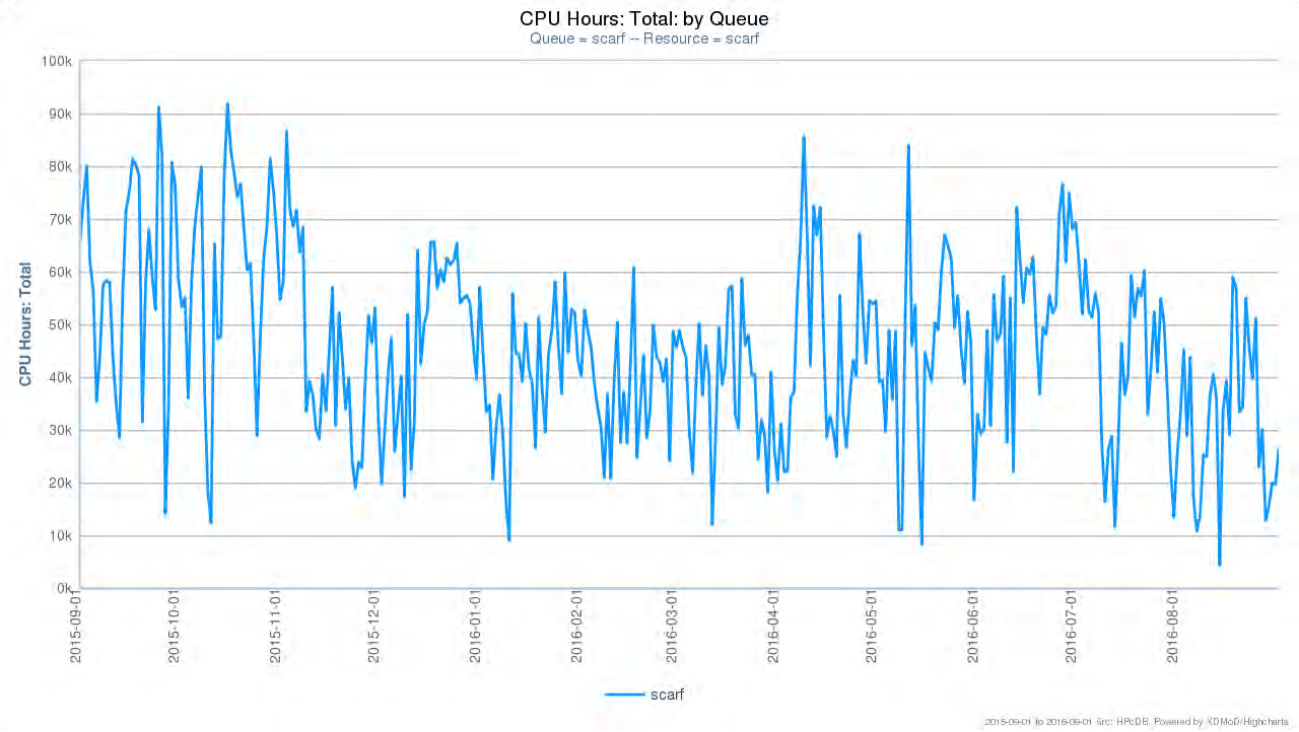

Figure 7.1.1: SCARF Queue Usage

We continue to use the mechanism inside LSF to allow groups of users to get preferential access to portions of hardware they have contributed money to purchase, while still making the hardware available to other users' jobs up to 24 hours in length. This is currently in place for ISIS on SCARF13 and ISIS and CLF FBI on SCARF14 and SCARF15

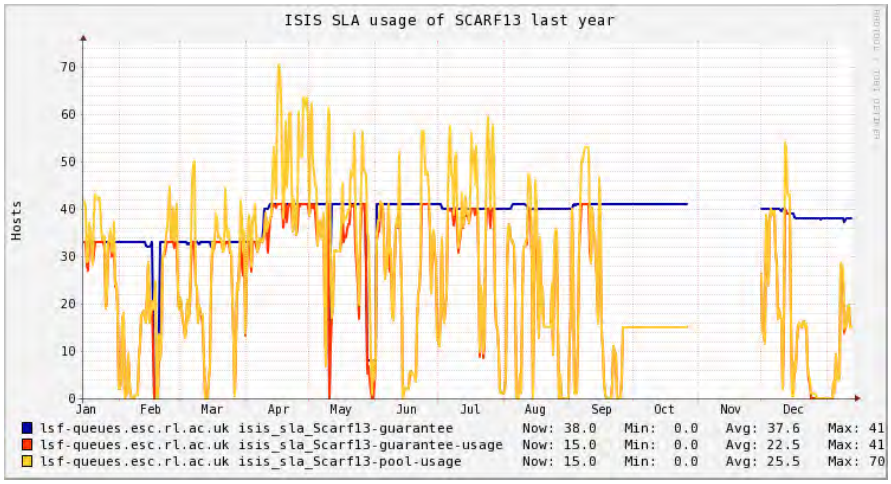

Figure 7.1.2: ISIS SLA Usage of SCARF 13

The blue line shows the level that is guaranteed to ISIS on SCARF13. The red line shows ISIS usage of their guarantee. The yellow line shows all ISIS usage. While usage varies over the year the

average for the yellow line is close to the guaranteed figure, showing that on average ISIS are making use of the hosts they get priority access to.

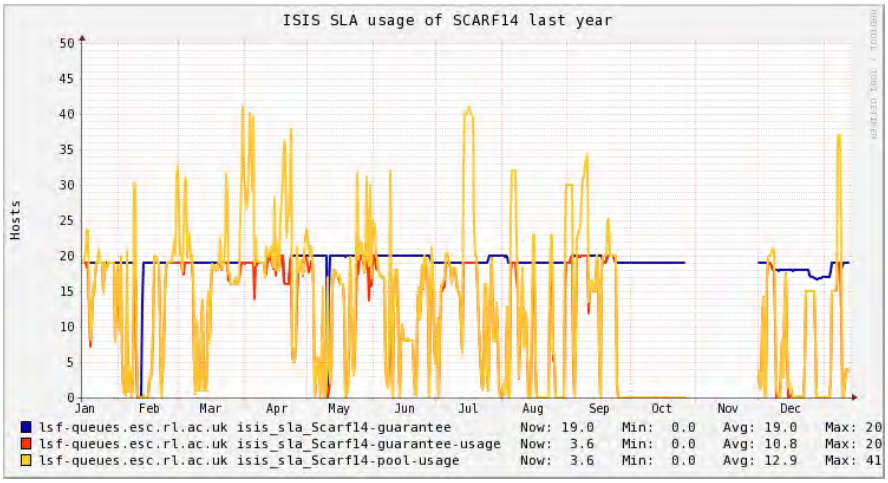

Figure 7.1.3: ISIS SLA Usage of SCARF 14

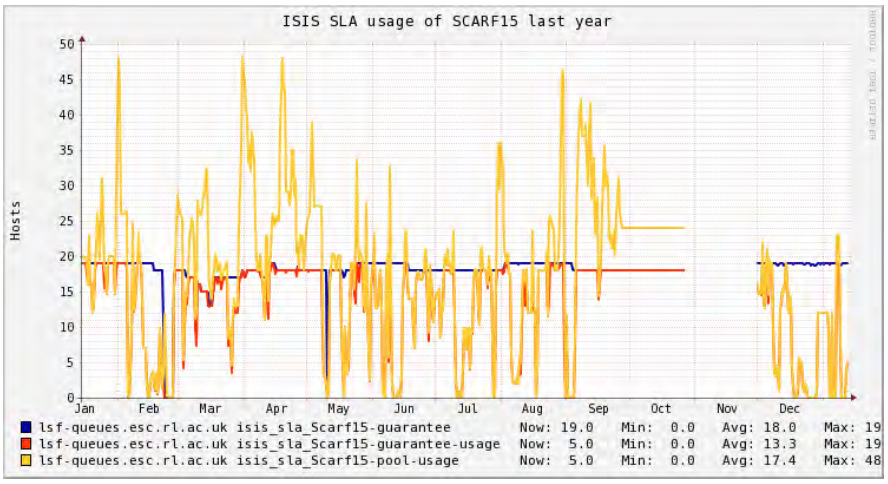

Figure 7.1.4: ISIS SLA Usage of SCARF 15

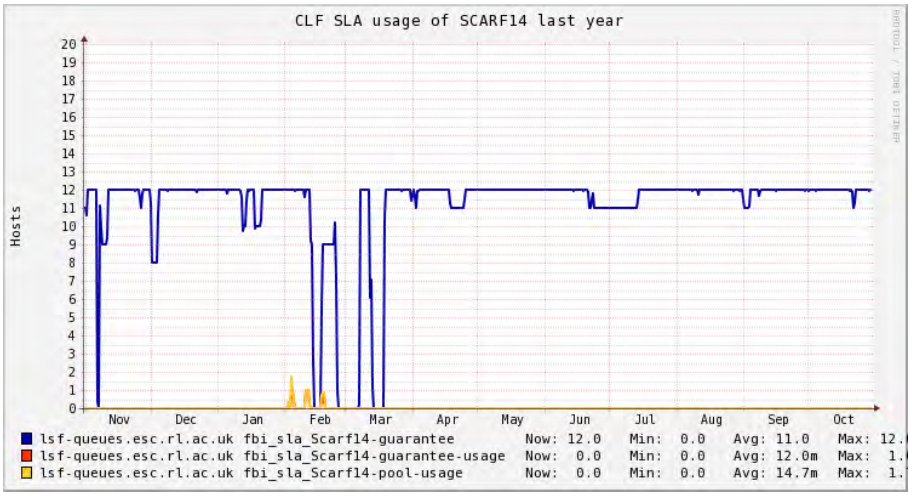

Figure 7.1.5: CLF SLA Usage of SCARF 14

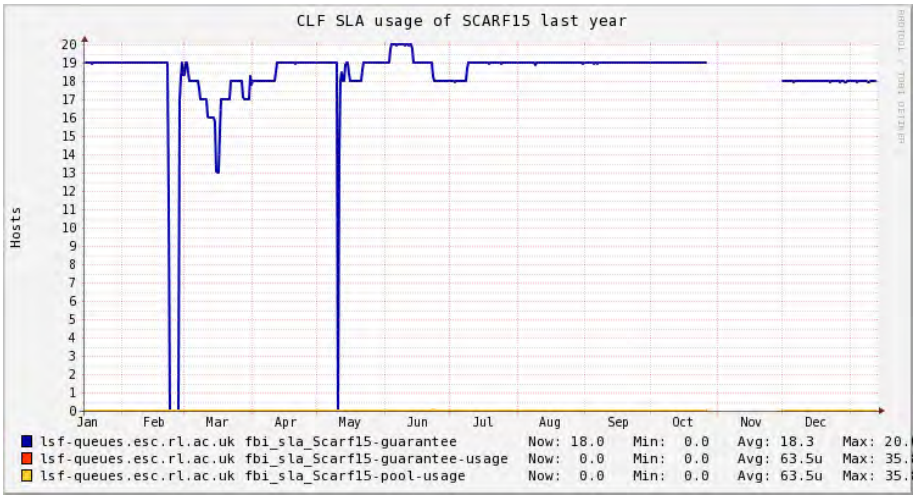

Figure 7.1.6: CLF SLA Usage of SCARF 15

The SCARF14 and SCARF15 plots for CLF FBI show that they have not yet begun making extensive use of their guaranteed resources

7.2 SCARF-Lexicon, MagnaCarta and Lexicon2 Queues

These queues are primarily for CLF Plasma Physics use. The Lexicon 1 nodes with 256 cores were traded in for additional cores from the SCARF16 cores, increasing the size of the new cluster to 480 cores. To reflect this new capacity the cluster was renamed MagnaCarta. Lexicon2 has 544 cores purchased in 2010.

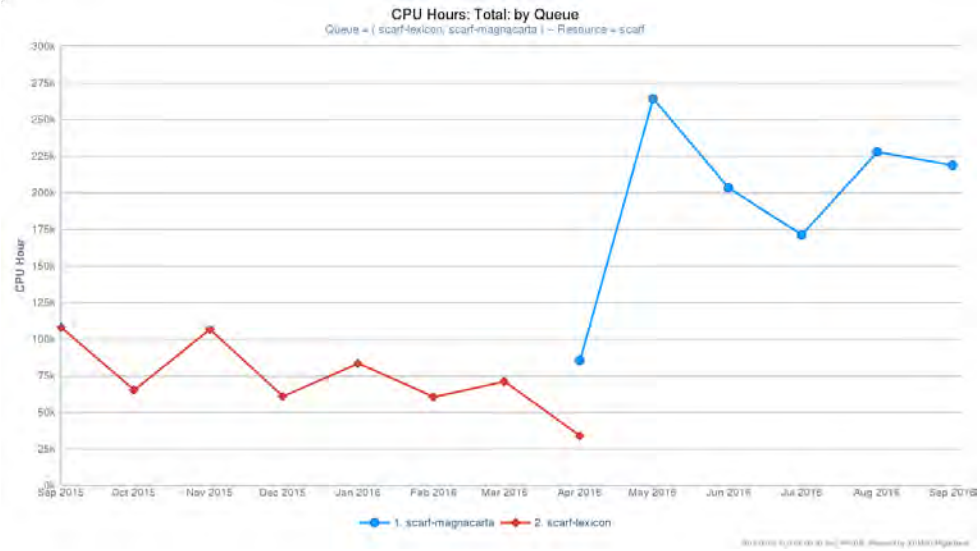

Figure 7.2.1: SCARF-Lexicon and SCARF-MagnaCarta Usage

The graph for the SCARF-Lexicon and SCARF-MagnaCarta queues shows significant usage, as they are available to CLF external collaborators.

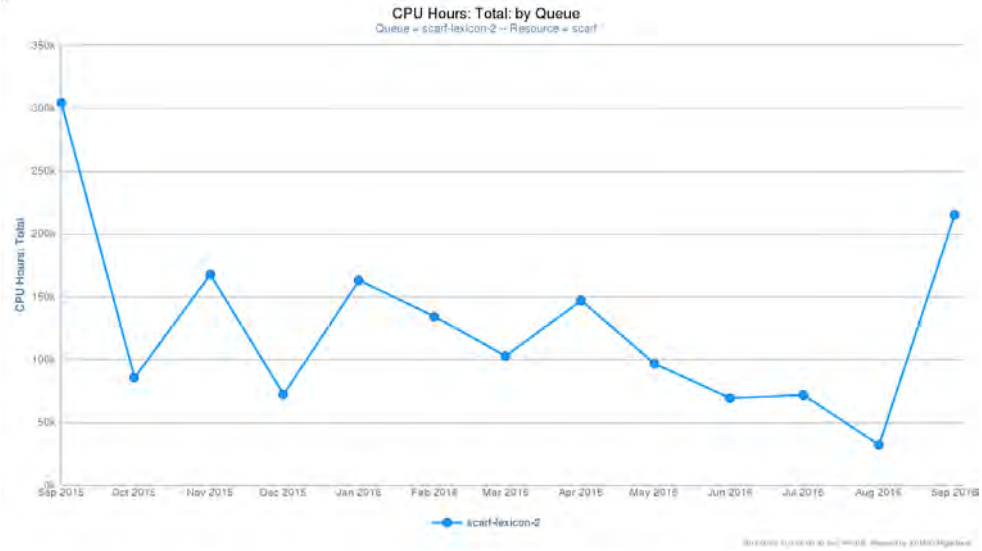

Figure 7.2.2: : SCARF Lexicon-2 Usage

SCARF-Lexicon-2 continues to be used for higher priority Lexicon/MagnaCarta users and on demand to support CLF experiments.

7.3 SCARF-IBIS

SCARF-IBIS has a capacity of 240 CPU cores.

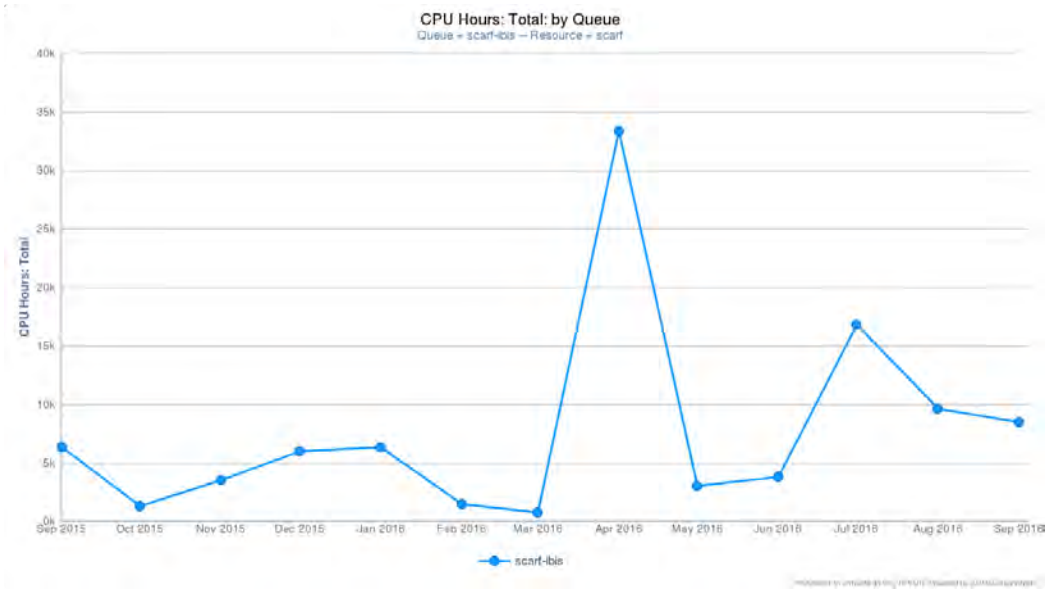

Figure 7.3.1: SCARF-IBIS Usage

7.4 SCARF Total Power draw (amps)

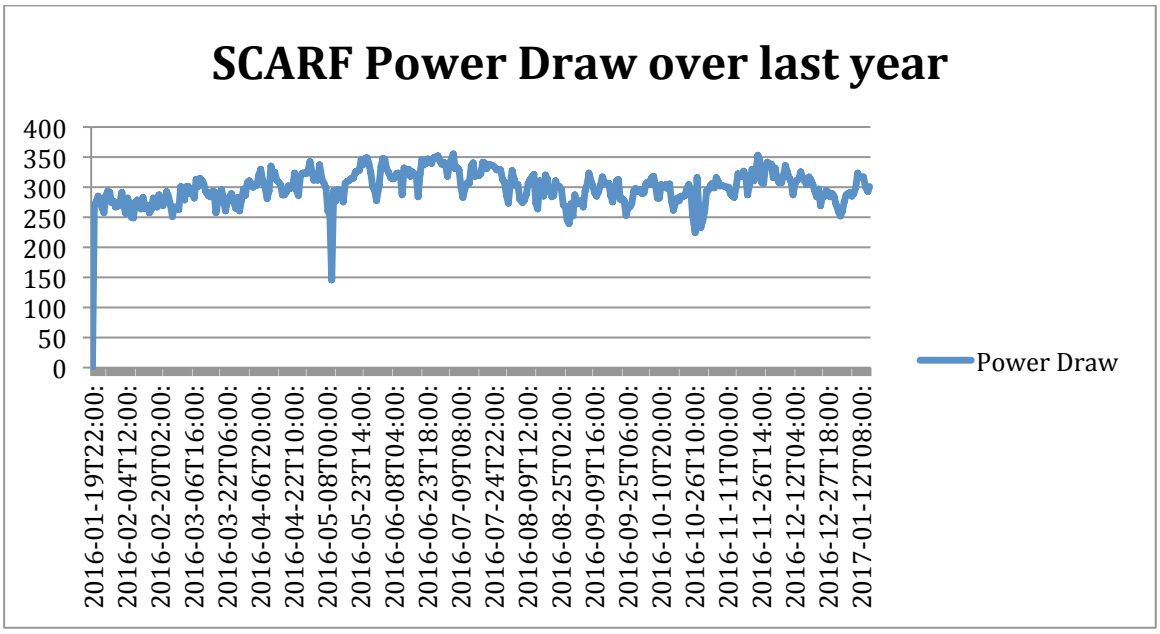

Figure 7.4.1: SCARF Power Usage

The approximate average power draw of the SCARF cluster (including Lexicon) is about 300 amps or 72 kW. This excludes the power needed to cool, pump and move cold air. The efficiency of SCARF in terms in Gflops/W is giving in the table below.

Year Purchased	Gflops/W
2010	0.32
2011	0.48
2012	0.50
2013	0.59
2014	0.98
2015	1.95
2016	1.95

Figure 7.4.2: GFlops/W for SCARF generations of equipment

From the above table it is clear that the Gflops/W achieved increase per generation of the SCARF equipment. SCARF16 is the same hardware as SCARF15. This supports the continual refresh rate of SCARF hardware rather than a big bang approach.

7.5 Filesystem Usage

The plot below outlines the use of the Panasas filespace on the SCARF service. The filespace is shared across a number of projects therefore not all space is available to SCARF users, but SCARF users benefit as increasing the amount of space also increases the bandwith to the storage as files are redistributed around the Panasas system automatically.

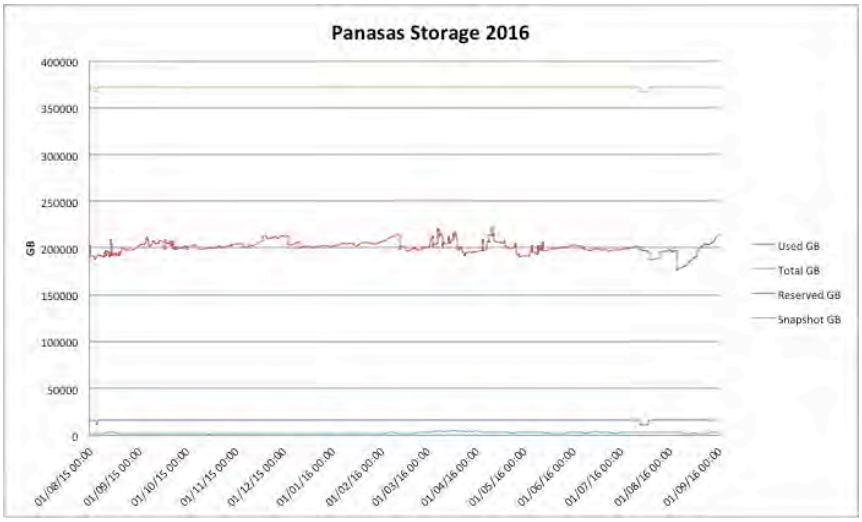

Figure 7.5.1: Filespace usage on the Panasas Storage

7.6 Networking

The diagram below shows the SCARF compute clusters embedded in the larger Research Infrastructure group's networking infrastructure. A change that has been taking place gradually has been the migration of SCARF equipment one step away from the core RIG network infrastructure to the switch labelled "HPC switch" in the diagram. This was necessary as the latest SCARF hardware now has faster host connections – up from 1 gigabit to 10 gigabit, which means that a faster uplink

is required to cope with the greater bandwidth demands from that equipment. As the faster host connections will become the new default, additional network capacity was required.

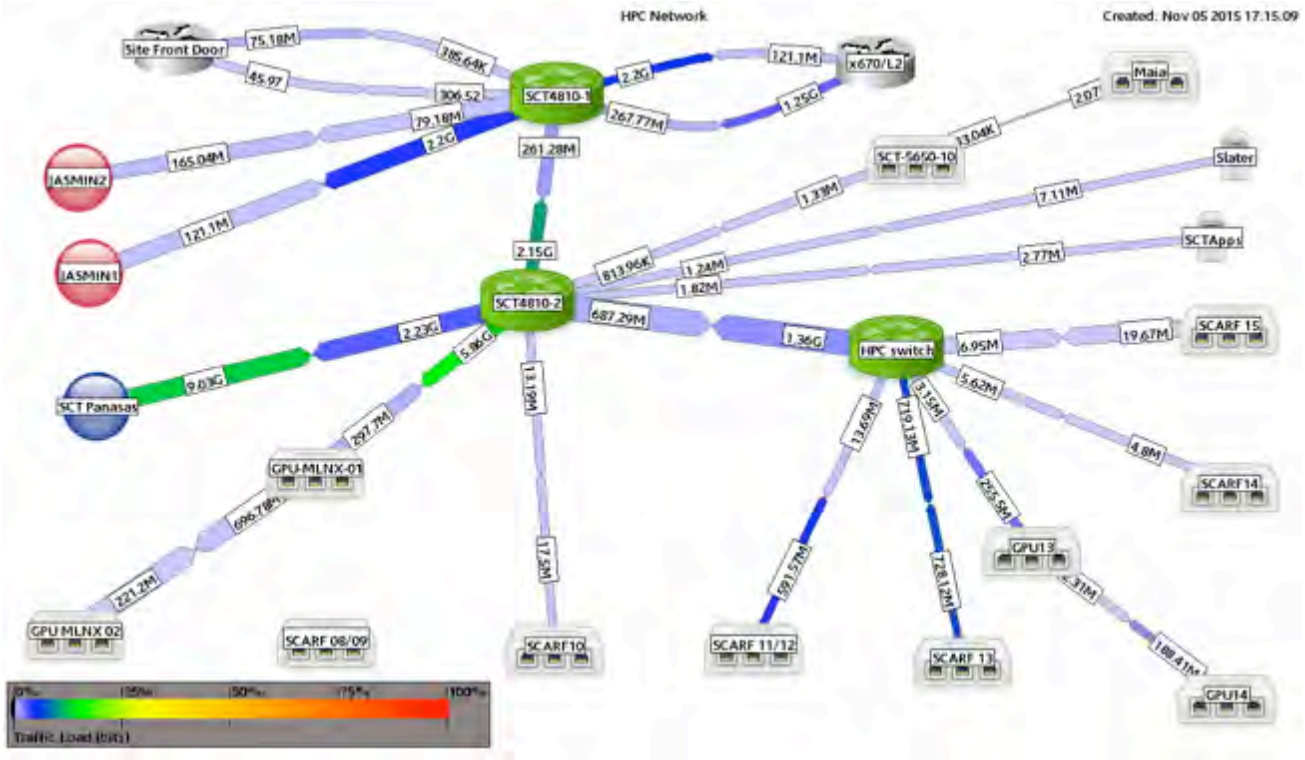

Figure 7.6.1: SCARF Network Topology

8 APPENDIX: SCARF DEVELOPMENTS

It has been a busy year for the SCARF service. Users' will have noticed most impact with the additional of capacity and upgrades to applications. However, a lot of effort goes into improving the management of SCARF.

8.1 Technical Developments

- In April 2016 the hardware tranche of dual Intel E5-2650v3, providing 1120 cores was made available.
- The underlying batch system was upgraded in September from version 8.0 to 10.1 to allow newer operating systems to be used

8.2 Application Stack

A selection of new or updated applications is in the table below:

Application	Area	Version
netCDF	Data model, library, and file format for storing and managing data	4.4.1
GNU compiler	Fortran, C, C++ compilers and Maths libraries	5.3.0
Intel compiler	Fortran, C, C++ compilers and Maths libraries	17.0
PGI compilers	Fortran, C, C++ compilers and Maths libraries	15.9
CASTEP	Computational Chemistry	16.1
Avizo	3D analysis software for scientific and industrial data	9.0.1

Figure 8.2.1: SCARF Application Stack

A full list of the available software on SCARF can be found on the SCARF website: http://www.scarf.rl.ac.uk/applications-libraries